RESEARCH ARTICLE SUMMARY

NEUROSCIENCE

Chromatin plasticity predetermines neuronal eligibility for memory trace formation

Giulia Santoni, Simone Astori, Marion Leleu, Liliane Glauser, Simon A. Zamora†, Myriam Schioppa, Isabella Tarulli, Carmen Sandi, Johannes Gräff*

INTRODUCTION: During development, epigenetic heterogeneity gives rise to different cell types with different functions. By stably instructing the activation and deactivation of genomic loci to catalyze specific signaling cascades, epigenetic mechanisms play a pivotal role in lineage commitment and cellular differentiation. What remains elusive, however, is whether chromatin plasticity plays an equally important role in the development of dynamic functions in fully differentiated cells, such as adult neurons. One of the most intriguing features of neurons is their capacity for information encoding. Notably, for each new piece of information memorized the brain deploys only a subset of its neurons, implying that even within the same developmentally defined cell type, not all neurons are equally fit for information encoding at any given time.

RATIONALE: The dependence of memory formation on neuronal selection made us ask whether chromatin architecture might be heterogenous enough, among otherwise seemingly homogeneous cellular identities, to drive information encoding. And specifically, whether enhanced chromatin plasticity could be a catalyst force to prime neurons to be preferentially selected for memory formation.

RESULTS: Focusing on the mouse lateral amygdala, a key brain region responsible for the encoding of associative forms of memory, we discovered that its excitatory neurons indeed exhibit heterogeneous chromatin plasticity, and further, that those preferentially recruited into learning-activated neurons were enriched for hyperacetylated histones, an abundant epigenetic modification in the brain. To functionally test this correlation between chromatin plasticity and information encoding, we subsequently manipulated histone acetylation levels by either increasing or decreasing histone acetyltransferases (HATs) in these neurons. We found that a gain-of-function of histone acetylation-mediated epigenetic plasticity facilitated neuronal recruitment into the memory trace whereas a loss-of-function thereof prevented memory allocation.

Interested in the molecular mechanisms underlying this selection, we next performed single nucleus multiome sequencing for the simultaneous assessment of chromatin accessibility and gene expression changes occurring in the epigenetically modified neurons. These results revealed gained chromatin accessibility or increased expression at genomic locations closely related to structural and synaptic plasticity, as well as to neuronal excitability, which

has been identified as an important phy logical process for information encoding. Check for updates cordingly, we found that increasing chromatin plasticity also led to an increase in intrinsic neuronal excitability and promoted structural and functional synaptic remodeling.

For a process to be truly qualified as influencing memory allocation, it should also support memory retention. To this end we tested the HATinjected mice on Paylovian fear conditioning, an associative type of memory, and found that they displayed a significantly stronger fear memoryan effect that lasted for up to eight days. Notably, optogenetic silencing of the epigenetically altered neurons prevented fear memory recall, suggesting a cell-autonomous relationship between chromatin plasticity and memory trace formation. Lastly, by combining Förster resonance energy transfer (FRET) tools and calcium imaging in single neurons, we revealed that the nexus between chromatin plasticity and intrinsic neuronal excitability occurs endogenously, cell-autonomously, and in real time.

CONCLUSION: Our findings show that a neuron's eligibility to be recruited into the memory trace depends on its epigenetic state prior to learning, and thereby identify chromatin plasticity as a novel form of plasticity important for information encoding. A neuron's epigenetic landscape might therefore represent an adaptable template so as to register and integrate environmental signals in a dynamic, yet long-lasting manner.

The list of author affiliations is available in the full article online. *Corresponding author. Email: johannes.graeff@epfl.ch

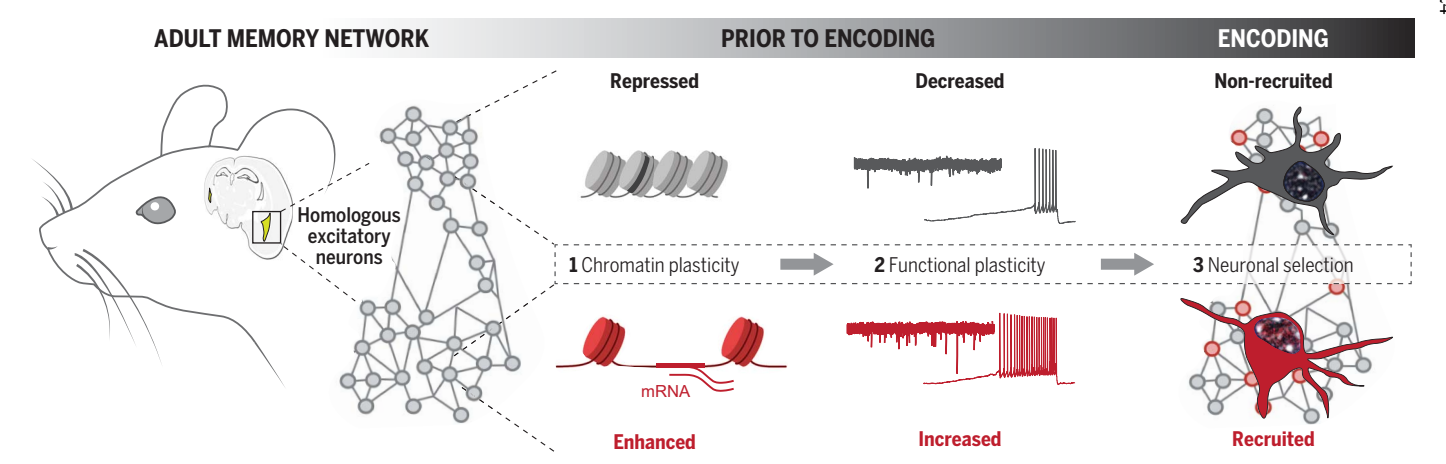
†Present address: Champalimaud Research, Champalimaud Centre for the Unknown, Lisbon, Portugal.

Cite this article as G. Santoni et al., Science 385, eadg9982 (2024). DOI: 10.1126/science.adg9982



READ THE FULL ARTICLE AT

https://doi.org/10.1126/science.adg9982



Chromatin plasticity favors information encoding. In the adult brain, neurons pertaining to the same developmentally defined cell type intrinsically display heterogeneous levels of chromatin plasticity, the enhancement of which favours transcriptional and electrophysiological signatures that promote neuronal recruitment into the memory trace.

RESEARCH ARTICLE

NEUROSCIENCE

Chromatin plasticity predetermines neuronal eligibility for memory trace formation

Giulia Santoni¹, Simone Astori², Marion Leleu³, Liliane Glauser¹, Simon A. Zamora¹†, Myriam Schioppa^{1,4}, Isabella Tarulli¹, Carmen Sandi², Johannes Gräff¹*

Memories are encoded by sparse populations of neurons but how such sparsity arises remains largely unknown. We found that a neuron's eligibility to be recruited into the memory trace depends on its epigenetic state prior to encoding. Principal neurons in the mouse lateral amygdala display intrinsic chromatin plasticity, which when experimentally elevated favors neuronal allocation into the encoding ensemble. Such chromatin plasticity occurred at genomic regions underlying synaptic plasticity and was accompanied by increased neuronal excitability in single neurons in real time. Lastly, optogenetic silencing of the epigenetically altered neurons prevented memory expression, revealing a cell-autonomous relationship between chromatin plasticity and memory trace formation. These results identify the epigenetic state of a neuron as a key factor enabling information encoding.

neuron's identity arises from lineage commitment during development through stable chromatin remodeling (1). For many cognitive processes, however, only a subset of seemingly identical neurons is engaged (2, 3), which begs the question of whether a finer-grained chromatin plasticity could dictate which neurons are eligible for specialized brain functions within a developmentally defined neuronal niche. Memory allocation is one cognitive process that depends on neuronal selection (4, 5), because the network of cells storing a given memory is only a small percentage of the total number receiving similar inputs. Selective neuronal recruitment into the encoding ensemble depends on somatic plasticity such as intrinsic excitability (IE) (6, 7), but it remains unknown whether and to what extent nuclear plasticity at the chromatin level contributes to neuronal selection for information encoding.

Results

LA neurons display intrinsic chromatin plasticity that correlates with memory allocation

To investigate this question, we focused on the mouse lateral amygdala (LA), a critical site of synaptic plasticity during Pavlovian fear learning (8,9). We first assessed whether chromatin

¹Laboratory of Neuroepigenetics, Brain Mind Institute, School of Life Sciences, Ecole Polytechnique Fédérale de Lausanne, 1015 Lausanne, Switzerland. ²Laboratory of Behavioural Genetics, Brain Mind Institute, School of Life Sciences, Ecole Polytechnique Fédérale de Lausanne, 1015 Lausanne, Switzerland. ³Bioinformatics Competence Center, Ecole Polytechnique Fédérale de Lausanne, 1015 Lausanne, Switzerland. ⁴The institute of Medical Sciences, School of Medicine, Medical Sciences and Nutrition, University of Aberdeen, Aberdeen A825 2ZD, UK.

*Corresponding author. Email: johannes.graeff@epfl.ch †Present address: Champalimaud Research, Champalimaud Centre for the Unknown, Lisbon, Portugal. compaction in LA principal neurons displays endogenous heterogeneity, a necessary prerequisite to qualify as a driver of functional neuronal specialization. We measured the neuronal content of heterochromatin protein-1 (HP1-β), which is involved in the maintenance of transcriptionally silent heterochromatin (10), by immunohistochemistry in CaMKIIa neurons (fig. S1, A and B), the major cell type in the LA. This was done one hour after an auditory fear conditioning (aFC) task, which induces memory retention (fig. S1C), as well as in a home cage (HC) control group, which served as a reference for the epigenetic disposition at baseline (Fig. 1, A and B). We found that LA cells exhibited a wide range of HP1-β levels, indicating intrinsic heterogeneity in chromatin compaction (Fig. 1D and fig. S1D). What is more, we observed a substantial reduction in HP1-β content following aFC (Fig. 1, D and E), suggesting that fear learning induces overall chromatin relaxation.

Next, to evaluate whether such chromatin relaxation might influence memory allocation, we assessed HP1- β expression in the population of cells positive for cFos, an immediate early gene (IEG) marker of neuronal activity that identifies putative engram cells (11, 12). After aFC, the cFos positive (cFos+) ensemble was markedly increased in size (Fig. 1F), confirming that the LA is actively engaged by aFC. However, we did not find any specific difference in heterochromatin content between cFos+ and cFos negative (cFos-) cells (Fig. 1, G and H, and fig. S1E).

Therefore, using the same experimental settings, we next characterized histone acetylation (Fig. 1, A and C), a major regulator of chromatin plasticity that occurs on specific aminoacid residues of histone core proteins

(13-16). We focused our analysis on the acetylation of two sites, that of histone 3 on lysine 27 (H3K27Ac) and H4K5Ac, both of which are induced by neuronal activation and follow memory formation (17, 18). Similar to HP1-β, we observed endogenously occurring heterogeneity in histone acetylation in LA principal neurons (fig. S1, F and G). In contrast to HP1-β, aFC did not change the overall distribution of H3K27Ac and H4K5Ac levels (Fig. 1, I, J, N, and O). However, when we analyzed histone acetylation within cFos+ neurons we found a significant enrichment in H3K27Ac but not H4K5Ac, compared with cFos-cells (Fig. 1, K, L, M, P, and Q, and fig. S1H). These changes were specific to associative learning because mice undergoing an immediate shock deficit paradigm-a nonassociative experiencedid not show an increase in the cFos+ ensemble size nor an enrichment in H3K27ac (fig. S2). These findings suggest that although a salient experience such as aFC can promote overall chromatin relaxation within the LA, within specific cell ensembles different epigenetic modifications are at play to delineate their specialized function.

HAT overexpression increases H3K27Ac and favors memory trace allocation

To test whether LA principal neurons enriched for H3K27ac may be predisposed for memory trace recruitment, we subsequently manipulated histone acetylation levels. Histone acetylation is regulated by the opposing action of histone deacetylases (HDACs) and histone acetyltransferases (HATs), the latter of which is composed of 18 different proteins (19, 20). To experimentally increase H3K27ac, we overexpressed two members of the phylogenetically opposite poles of the HAT family, CREB-binding protein (CBP) and Lysine acetyltransferase 5 (KAT5) (21) (Fig. 2A). Lentiviruses carrying CBP, KAT5 or a control eGFP reporter under the CaMKIIa promoter were bilaterally injected into the LA; following this, mice underwent the same aFC task as before. All inserts were fused to a Myc-Flag tag for nuclear visualization, and eGFP served to facilitate the identification of the injection site (Fig. 2B). Both CBP and KAT5 overexpression led to elevated H3K27Ac levels one hour after aFC as well as in the HC control group (Fig. 2, C to E, and fig. S3, A to F), including within cFos+ cells in both the aFC and the HC group (Fig. 2, F and G).

We then examined whether such altered histone acetylation affected the propensity of neurons to become part of the encoding ensemble, i.e., memory allocation. cFos+ neurons were preferentially recruited to the HAT-infected fraction following aFC (Fig. 2, H and I), whereas no such difference was observed in the HC group (Fig. 2J). This was not due to a size change of the encoding ensemble (Fig. 2K),

Fig. 1. Neurons recruited into the encoding ensemble display elevated H3K27Ac levels. (**A**) Experimental design to study LA chromatin plasticity. Adult wild-type (WT) mice were assigned to either an HC or aFC group and processed for immunohistochemistry 60 min after the behavioral episode. (**B**) LA nuclei stained for Hoechst (white), CaMKlla (orange), HP1-β (green), and cFos (red) after aFC; scale bars 10 μm. (**C**) LA nuclei stained for Hoechst (white), H3K27Ac (pink), H4K5Ac (orange) and cFos (red) after aFC; scale bars 10 μm. (**D**) Normalized HP1-β intensity values of individual CaMKlla positive (CaMKlla+) neurons for HC and aFC. (**E**) Per-mouse average of normalized HP1-β intensity values in CaMKlla+ neurons for HC and aFC. n = 4 mice per group. (**F**) Ensemble size calculated as per-mouse average of double positive cFos+/CaMKlla+ cells for HC versus aFC. (**G**) Frequency distribution of nuclei expressing HP1-β represented by bins in cFos- versus cFos+/CaMKlla+ neurons, at aFC. (**H**) Per-mouse average of normalized HP1-β intensity values in cFos- versus cFos +/CaMKlla+, after aFC. (**I** and **N**) Normalized H3K27Ac (I) and H4K5Ac (N)

intensity values of individual neurons for HC and aFC. (**J** and **0**) Per-mouse average of normalized H3K27Ac (J) or H4K5Ac (O) intensity values for HC and aFC. n=6 to 8 mice per group. (**K**) Ensemble size calculated as per-mouse average of double positive cFos+/CaMKlla cells for HC versus aFC. (**L** and **P**) Frequency distribution of nuclei expressing H3K27Ac (L) or H4K5Ac (P) represented by bins in cFos- versus cFos+/CaMKlla+ neurons, after aFC. (**M** and **Q**) Per-mouse average of normalized H3K27Ac (N) or H4K5Ac (R) intensity values in cFos- versus cFos+ neurons after aFC. The significant difference between nuclear distributions (D, I, N, G, L, and P) was tested with an unpaired two-tailed Kolomogorov-Smirnov test at P-value < 0.01. Statistical difference comparing per-mouse values (E to F; J to K and O) was measured by an unpaired two-tailed Kolomogorov-Smirnov test set at P-values < 0.05. Intramouse matched averages (H, M, and Q) were tested for significant difference with a paired two-tailed Wilcoxon test, set at P-values < 0.05. For all tests: *, $P \le 0.05$; **, $P \le 0.01$; ****, $P \le 0.001$; ****, $P \le 0.001$; ****, $P \le 0.001$; *****, $P \le 0.0001$.

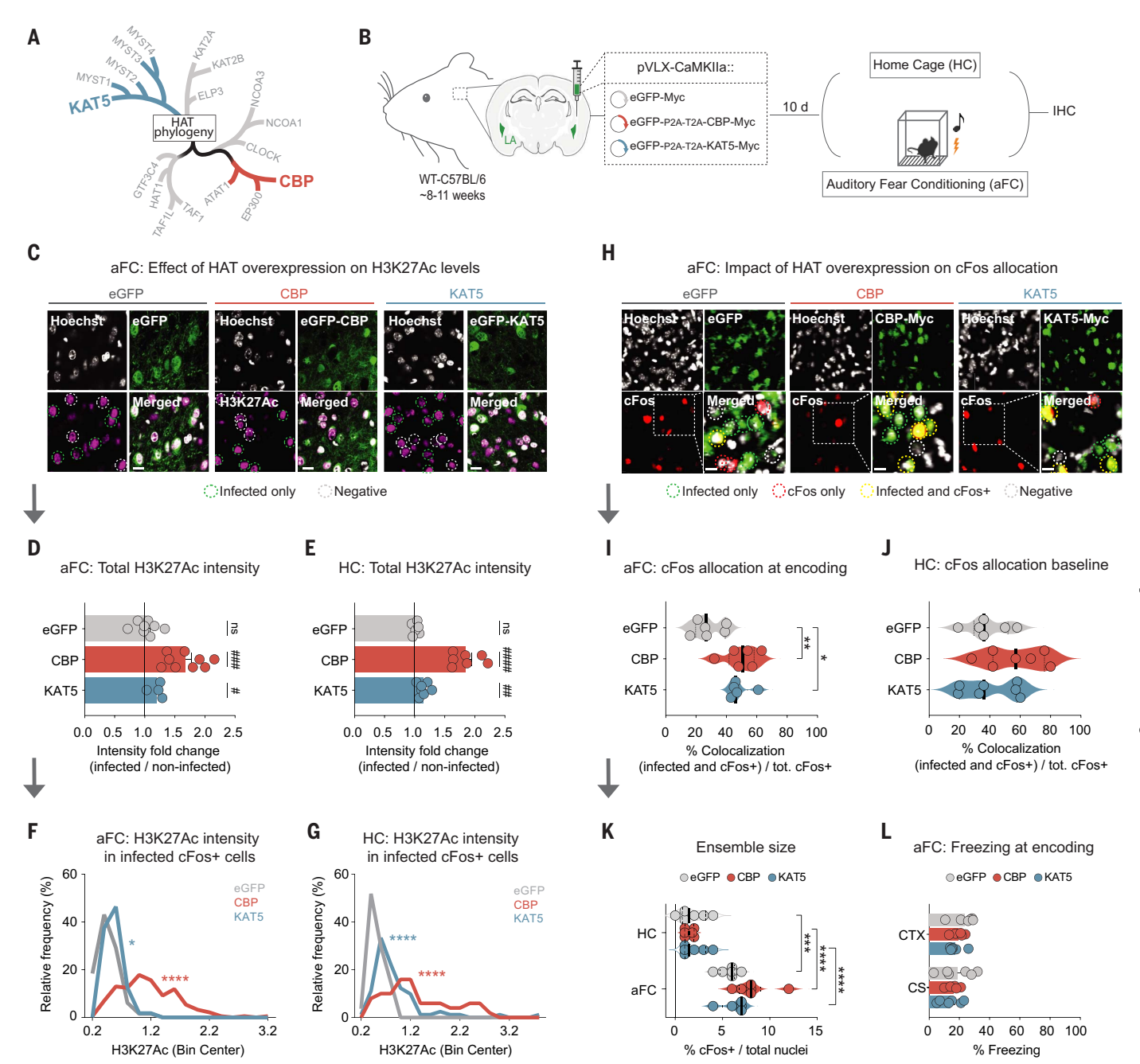


Fig. 2. HAT overexpression increases H3K27Ac levels and favors memory allocation. (**A**) HAT family phylogeny with HATs CBP and KAT5 highlighted. Modified, with permission, from (*21*). (**B**) Experimental design. The LA of adult WT mice was bilaterally injected with lentiviruses carrying eGFP, CBP, or KAT5. After 10 days, mice were assigned to a HC or aFC cohort and processed for immunohistochemistry 60 min later. (**C**) Colocalization images of LA nuclei stained for Hoechst (white), eGFP (green), and H3K27Ac (purple), scale bars $10\mu m$. (**D** to **E**) Fold change of H3K27Ac levels in infected versus noninfected neurons for aFC (D) and HC (E). Hashtags represent *P*-values of two-tailed one-sample *t* tests comparing the difference to 1, which represents H3K27Ac levels of the noninfected control neurons. (**F** to **G**) Frequency distribution of nuclei expressing H3K27Ac represented by bins in cFos+ infected neurons for aFC (F) and HC (G). Statistical significance was measured by the Kruskal-Wallis test (*P* < 0.0001), followed by Dunn's multiple comparisons test between

groups. (**H**) Colocalization images of LA nuclei stained for Hoechst (white), eGFP (green), and cFos (red) following aFC. Scale bars, 10 μ m. (**I** to **J**) Recruitment of the infected population into the cFos ensemble at aFC and HC. Kruskal-Wallis test [P < 0.0023 in (I), P < 0.2173 in (J)], followed by Dunn's multiple comparisons test comparing CBP and KAT5 percentages to the eGFP control group. (**K**) Ensemble size (measured as percent cFos+/total nuclei) across behavioral cohorts between experimental groups [two-way analysis of variance (ANOVA); (F) (1, 29) = 113.8, P = < 0.0001)]. Asterisks represent the P-values of the Šídák test when comparing, within each experimental condition, the cFos+ ensemble at HC versus aFC. (**L**) Baseline freezing levels measured at aFC during contextual exploration and tone exposure. Data are represented as mean \pm s.e.m. Each circle is an average value reported per mouse, n = 4 to 9 mice per group. For all tests: */#, $P \le 0.05$; **/##, $P \le 0.01$; ****/####, $P \le 0.001$; ****/####, $P \le 0.001$; n, not significant.

nor to a difference in baseline freezing behavior (Fig. 2L), nor to altered infection rates (fig. S3, G to I). Furthermore, this effect was specifically mediated by the HAT domain of CBP and KAT5, because overexpressing catalytically dead mutants (HATDM) did not alter memory allocation (fig. S4, A to I). Conversely, when we overexpressed HDAC2, a class I HDAC (22), memory allocation was left unchanged (fig. S4, J to P). Lastly, when we decreased H3K27ac levels by overexpression of shRNAs against CBP, memory allocation was reduced (fig. S5), indicating that elevated histone acetylation favors memory allocation.

HAT overexpression induces epigenetic and transcriptional changes at IE and synapse-related genes

Next, we examined by which epigenetic and transcriptional mechanisms HAT overexpression (OE) may facilitate memory allocation. Mice were injected with CBP, KAT5, or eGFPcontaining lentiviral vectors, and 10 days later LA nuclei were isolated and characterized by single nucleus (sn) multiome sequencing for the simultaneous assessment of their chromatin accessibility (snATAC-seq) and gene expression (snRNA-seq) changes (Fig. 3A). This experiment was performed in the HC cohort as we hypothesized that in order to be preferentially recruited upon memory encoding, HAT-infected neurons would carry specific epigenetic and transcriptional signatures already at baseline.

The three datasets showed comparable cell type composition (Fig. 3B and fig. S6A) and were characterized by the expected cell type ratios (of 80% excitatory versus 20% inhibitory neurons) excitatory neuron's subclustering (Fig. 3C and fig. S6, B to D) in the LA (23). Excitatory neurons were the cell type preferentially targeted by CamKII-driven viral constructs and therefore the population we explored in detail (Fig. 3D and fig. S6, E to G). Using the expression levels of cFos and other rapid IEGs (24, 25) we first classified LA excitatory neurons into active and inactive clusters (Fig. 3E and fig. S6, H to K) and studied the impact of HAT OE on those clusters. Irrespective of their activity state, HAT infection led to cluster separation suggesting that HAT OE induces transcriptional differences already at baseline (fig. S6, L and M). Similarly, although HAT OE did not yield any difference in chromatin accessibility globally (Fig. 3F) nor at constitutively transcribed locations such as housekeeping genes (Fig. 3G), HAT infection skewed the heterogeneous distribution of activity-related loci such as rapid IEGs toward higher accessibility states (Fig. 3H and fig. S6N), suggesting that HAT OE epigenetically primes cells toward activity.

But how precisely does HAT OE facilitate this transition toward activity? In the follow-

ing analysis, we focused on comparing infected neurons across experimental conditions (fig. S7A). Differential accessibility (DA) measurements between CBP-, KAT5-, and eGFPinfected neurons revealed that promoter elements mostly gained in accessibility (Fig. 3I and fig. S7, B and C), which further showed a high (>95%) overlap with H3K27Ac peaks (integrated from (18) (Fig. 3J), gain in accessibility of 1.5 to 2 upon CBP and KAT5 OE, respectively (Fig. 3K, and fig. S7, D and E). Accordingly, differential gene expression (DE) analysis found that HAT OE induced significant gene up-regulation with little down-regulation (Fig. 3L, fig. S7, F and G). Through a DA-DE intersection analysis, we observed a high functional overlap between gained promoter accessibility and transcriptional up-regulation, particularly at synapse-related ontologies (Fig. 3M and fig. S7H). Zooming in on the genes driving these enrichments we found that both HATs targeted locations closely related to structural and synaptic function, such synaptophysin (Syp), protein kinase C (Prkcg), calcium/calmodulindependent protein kinase 2b (Camk2b) or dematin actin binding protein (Dmtn), whereas others were related to neuronal excitability and firing such as calcium voltage-gated channel (Cacng3), sodium-dependent phosphate transporter (Slc17a7), glutamate receptor (Grin1), and glutamate receptor interacting protein 1 (Grip1) (Fig. 3N and fig. S7I).

However, at the individual gene level the HAT effect appeared to induce either DA or DE (Fig. 3N), with few showing both. To better understand the mechanism behind this dichotomy we inspected whether promoters that gained accessibility and genes that became upregulated upon HAT OE already exhibited a different ATAC signal at the transcriptional start site (TSS) in the eGFP condition. We found that genes undergoing transcriptional up-regulation upon HAT OE were characterized by an already accessible TSS at baseline (DE genes in Fig. 3O), whereas genes that gained in accessibility (but were not up-regulated) were characterized by a less accessible TSS (DA genes in Fig. 3O and fig. S8A). This gain in accessibility could either happen sharply at the TSS [DA@TSS, ±50 base pairs (bp)] or expand to regulatory sequences in the extended promoter region (DA≠TSS, see Materials and Methods) (Fig. 3, P and Q, and fig. S8, B and C). Which gain-in-accessibility scenario occurred was again dependent on the baseline chromatin state: DA@TSS genes were the ones most closed at baseline, whereas DA≠TSS genes exhibited permissive TSS accessibility comparable to DE genes (Fig. 3R). These differences in chromatin accessibility were also mirrored by distinct baseline expression levels, insofar that genes with a more permissive TSS showed higher transcriptional activity than closed promoters (Fig. 3, S and T, and fig. S8, D to F). Finally, while DE and DA \neq TSS genes showed similar transcription factor motif enrichment, DA@TSS were specifically enriched in FOS:: JUN and RXRG motifs, transcription factors previously implicated stimulus-dependent plasticity (26, 27) and IE (28), respectively (fig. S8G).

HAT overexpression increases IE and induces synaptic remodeling

Since HAT OE induced epigenetic and transcriptional plasticity at loci associated with IE and synaptic function, we next examined whether there are functional changes that accompany these chromatin-templated effects. First, we measured neuronal IE, a key somatic feature governing memory allocation (29-31). We bilaterally injected the LA with lentiviruses carrying CBP, KAT5, or a control eGFP reporter, 10 days after which the mice were prepared for ex vivo patch-clamp recordings (Fig. 4, A to D). In eGFP-injected mice, none of the measured IE parameters were altered in virally infected cells (Fig. 4, E and F, and fig. S10, A and B), indicating that the virus-based manipulation per se did not alter neuronal properties. By contrast, HAT OE affected several electrophysiological parameters indicative of increased IE: Both HATs increased the number of action potentials evoked by injections of depolarizing currents compared to noninfected neurons (Fig. 4, G and I), and HAT-infected neurons showed a decreased amplitude in the after-hyperpolarizing potential (Fig. 4, H and J), which defines the refractory period following an action potential (32, 33). Additionally, in CBP- (but not KAT5-) overexpressing cells. several other properties associated with an elevated IE profile were significantly altered, e.g., a decreased rheobase (fig. S10, C to F). Of note, HATDM-infected neurons showed no difference in any of the IE parameters (fig. S10,

Next, we asked whether HAT OE could also promote functional and structural remodeling at the synaptic level. Recordings of miniature excitatory postsynaptic currents (mEPSCs) revealed that LA neurons infected with CBP and KAT5 displayed an increased frequency of glutamatergic inputs, as indicated by the reduction in the mEPSCs interevent interval (Fig. 4, K to M). Conversely, mEPSC peak amplitude was comparable to noninfected cells (fig. S10, G, H, and I), suggesting no changes in postsynaptic AMPARs density prior to learning. Consistent with the electrophysiological data, HAT OE also increased spine density as compared to the eGFP-control condition (Fig. 4, N to P). These results show that chromatin plasticity directly acts on IE and synaptic remodeling in a cell-intrinsic manner and are well aligned with recent findings suggesting that the establishment of strong interconnectivity prior to learning favors the recruitment of cells into the memory network (34).

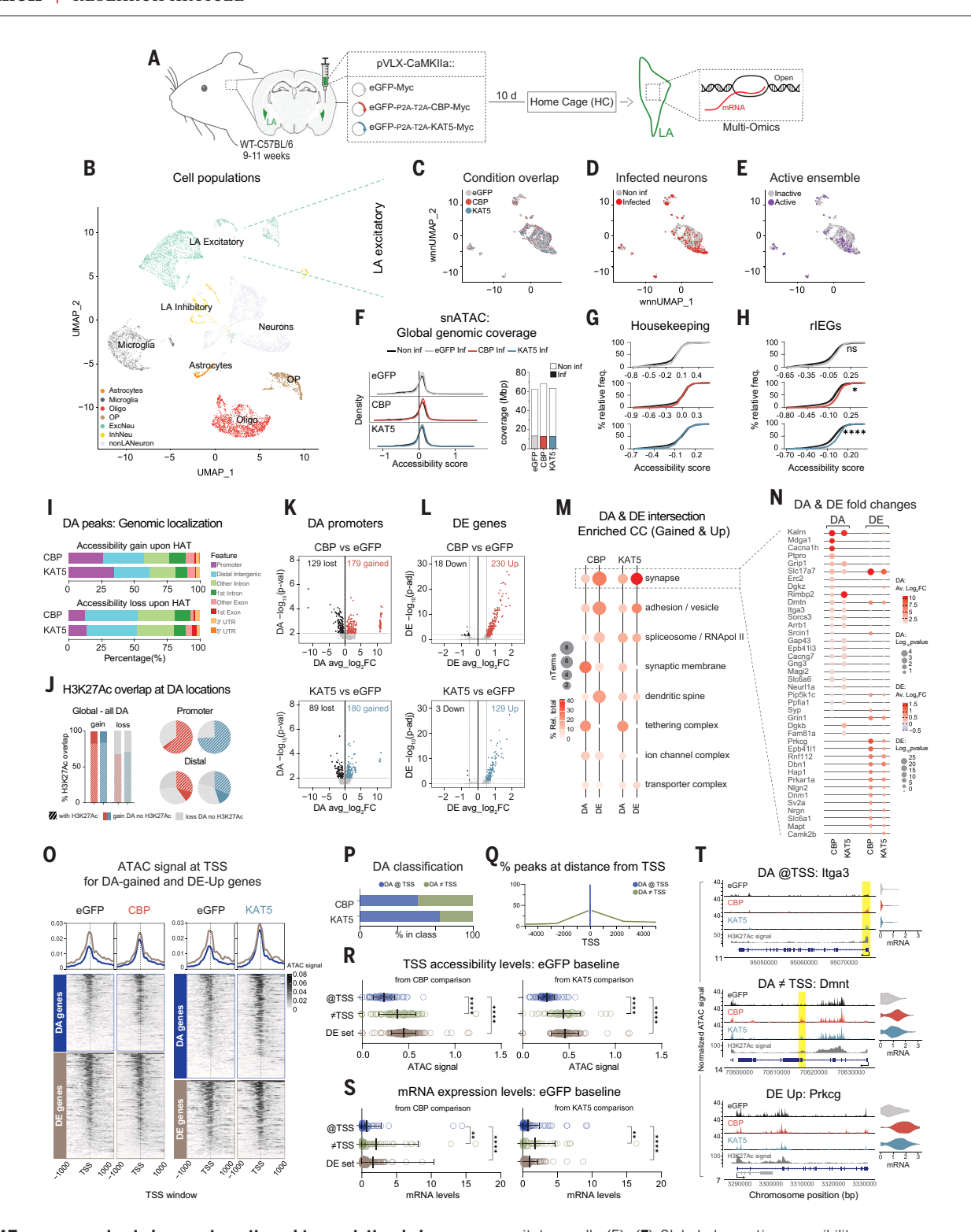


Fig. 3. HAT overexpression induces epigenetic and transcriptional changes at IE and synapse-related genes. (A) Experimental design: The LA of WT mice was bilaterally injected with lentiviruses carrying eGFP, CBP, or KAT5. After 10 days, brains were prepared for single nucleus multiomics-sequencing. (B) Pooled eGFP, CBP, and KAT5 datasets for mRNA-based UMAP clustering displaying the major LA cell types identified. Neuronal cells were further split according to their regional identity: LA-specific and non-LA-specific (light grey) and their main neuronal identities, excitatory and inhibitory. (C to E) ATAC and mRNA integrated UMAPs of LA excitatory neurons showing the overlap between eGFP, CBP, and KAT5 datasets (C), infected neurons (D) and active

excitatory cells (E). (**F**) Global chromatin accessibility coverage across experimental conditions as inferred from snATAC-seq-derived accessible regions identified in infected and noninfected neurons, visualized as accessibility score (left), and summed total coverage (right). (**G** and **H**) Accessibility scores for housekeeping (G) and rapid IEGs (H) gene sets between infected and noninfected neurons per condition. The distribution of accessibility scores was analyzed across groups using the Kruskal-Wallis test [P = 0.3815 in (**I**), P < 0.0001 in (**J**)], followed by Dunn's multiple comparisons test between groups. (I) Genomic locations of DA ATAC-peaks comparing CBP and KAT5-infected to eGFP-infected neurons. (J) Overlap between DA locations and

H3K27Ac signal derived from (18). (**K** and **L**) Volcano plots showing DA (K) and DE genes (L) in CBP (top) and KAT5 (bottom) infected excitatory neurons versus eGFP. (**M**) Summarized intersection analysis between the top 40 enriched GO terms [cellular compartment (CC)] derived from DA-gained and DE-up functional enrichments (fig. S7, E and G) (for expanded results see fig. S7H). Every circle represents the number of terms found per macro category and their incidence rate relative to the total terms in the dataset. (**N**) List of genes defining the GO-term categories contained in the "synapse" macro category. Every dot represents the fold-change difference in either DA-gained or DE-up datasets in CBP and KAT5 compared to eGFP-infected neurons; statistical significance is reported as Log_{10} *P*-value. (**O**) Heatmaps (bottom) and summary meta profiles (top) visualizing the ATAC signal distributions around the TSS (gene-centric approach) for all DA-gained and DE-up genes derived from the CBP and KAT5 versus eGFP comparisons. (**P**) Percent DA peaks classified in DA@TSS

and DA \neq TSS derived from CBP and KAT5 versus eGFP DA-gained datasets. (**Q**) Percentage of DA peaks found in the extended promoter region in DA@TSS and DA \neq TSS classes. (**R**) Average TSS ATAC signal in eGFP-infected excitatory neurons for the three gene classes (DA@TSS, DA \neq TSS, and DE-up) derived from CBP and KAT5 versus eGFP DA and DE comparisons. Statistical significance was measured by Kruskal-Wallis test (*P*-val. < 0.0001), followed by Dunn's multiple comparisons test between groups. (**S**) Average mRNA expression levels in eGFP infected excitatory neurons for the three gene classes (DA@TSS, DA \neq TSS, and DE-Up) derived from CBP and KAT5 versus eGFP DA and DE comparisons. Kruskal-Wallis test (*P*-val. < 0.0001), followed by Dunn's multiple comparisons test between groups. (**T**) Example coverage of genes from three classes: DA@TSS, DA \neq TSS, and DE-Up, and their relative average mRNA expression levels across eGFP-, CBP-, and KAT5-infected neurons. Data are represented as mean \pm s.d. For all tests: *, $P \le 0.05$; ***, $P \le 0.001$; ****, $P \le 0.001$; ****, $P \le 0.0001$.

HAT overexpression facilitates memory retention and optogenetic silencing of HAT-infected neurons disrupts it

For a process to be truly qualified as influencing memory allocation it should also support memory retention (4). To test this, we examined the effect of HAT OE in an aFC paradigm, in which we could not only test memory retention to the conditioned stimulus (CS+), but also the ability of the mice to discriminate against a nonconditioned stimulus (CS-) (Fig. 5, A and B). Both CBP- and KAT5-injected mice displayed a significantly higher freezing response 24 hours after encoding, and this increase in freezing was specific for the CS+ presentations (Fig. 5C and fig. S11A). Furthermore, when we retested a subgroup of these mice 8 days after encoding, both CBP- and KAT5injected mice still manifested an elevated freezing response during the CS+ epochs (Fig. 5D and fig. S11B), indicating improved long-term memory retention. We observed no differences in baseline freezing throughout the encoding phase (fig. S11C) nor in locomotor activity (fig. S11, D to G), excluding the possibility that the HAT OE-mediated increase in freezing was due to an unspecific increase in immobility. Moreover, the memory-promoting effect of HAT OE was specific to an associative component of the aFC, as HAT-overexpressing mice in the immediate shock paradigm did not show facilitated memory retention (fig. S11, H and I).

To causally examine whether HAT-overexpressing neurons are responsible for enhanced memory retention in a cell-intrinsic manner, we designed a viral system that allowed us to optogenetically inhibit the epigenetically altered neurons by expressing the inhibitory opsin ArchT under the same promoter as the HATs. These viruses were bilaterally injected in the LA, optic fibers were implanted, and 11 days later mice underwent the same aFC protocol (Fig. 5, E and F, and fig. S11J). During memory recall, we coupled the inhibitory photostimulation to half of the CS+ presentations, which allowed for a within-subject comparison of the freezing response during light OFF (no silencing) versus light ON (silencing) CS+ exposures (Fig. 5E). The analysis of the freezing behavior during the OFF-light epochs confirmed the strengthened fear response in HAT OE mice (Fig. 5, C and G). Conversely, optogenetic inhibition of HAT-overexpressing neurons blocked fear memory expression (Fig. 5H). By contrast, silencing a random population of LA neurons in control mice did not change the freezing response (Fig. 5H and fig. S11K).

IE and histone acetylation are cell-autonomously related at the single-cell level

The HAT OE experiments thus far have revealed a functional relationship between elevated histone acetylation levels and a neuron's eligibility for memory allocation and point to IE as an epigenetically templated effector process. To understand whether this relation reflects endogenously occurring mechanisms, we investigated the link between histone acetylation and IE at single-cell resolution in real time. We designed an approach merging the Förster resonance energy transfer (FRET) imaging technique of histone acetylation with a genetically encoded calcium indicator in primary neuronal cultures. For the former, we used the FRET probe Histac3 (35), which fluorescently reports histone acetylation levels in an inverse relationship: Only when histone acetylation is low do donor and acceptor molecules, which are situated on H3 and its reader bromodomain 4, respectively, enter into sufficiently close physical proximity to emit the FRET signal upon light excitation of the donor (Fig. 6A). For the latter, we used jRCaMP1b, a red-shifted, genetically encoded Ca²⁺ indicator that allows for measurement of Ca²⁺ transients at the singlecell level (36) (Fig. 6B). We measured FRET and Ca²⁺ signals before and after KCl stimulation, to study their relationship as a function of neuronal activity (Fig. 6, C and D).

Imaged neurons displayed a high degree of heterogeneity in histone acetylation (Fig. 6E and fig. S12A), coherent with the observation in the LA in vivo (fig. S1F). To relate histone acetylation to IE states, we subsequently focused our analysis on the most extreme FRET classes, LOW FRET and HIGH FRET (high and low acetylation content, respectively) (Fig. 6F

and fig. S12, B to D). While both LOW and HIGH FRET cells responded with elevated Ca²⁺ activity to neuronal activity (Fig. 6, G and H, and fig. S12E), LOW-FRET neurons showed a more sustained increase (Fig. 6I and fig. S12F). What is more, LOW-FRET neurons increased their activity in response to KCl earlier than HIGH-FRET cells, which showed a delayed time lag until ceiling (Fig. 6J and fig. S12G). Finally, LOW-FRET neurons expressed a significantly higher mean firing rate following neuronal activity (Fig. 6, K to M, and fig. S12, H and I), indicating that hyperacetylated neurons display a faster, stronger, and more stable increase in firing in cell-intrinsic manner.

Discussion

We found that a neuron's epigenetic makeup predetermines its eligibility to be recruited into the memory trace, which identifies a nuclear form of plasticity at the basis of sparse information encoding. By targeting somatic and synaptic effector mechanisms, such chromatintemplated plasticity is likely to govern the seemingly random nature of endogenous fluctuations in neuronal properties. Of note, we observed this nexus to occur cell-intrinsically and in real time, which delineates chromatin plasticity as a cell-autonomous feature influencing memory allocation. To further coordinate the sparsity of memory encoding, it is however likely that non-cell-autonomous mechanisms such as lateral inhibition (37, 38) are also at play. Although this prediction remains to be formally tested, it is supported by the observation that HAT OE did not alter the overall ensemble size (Fig. 2K) and that the altered epigenetic and transcriptional (fig. S6, J to M) and IE (Fig. 4, E to M) profiles were specific to the infected neurons. Despite using two phylogenetically distant HATs, their most pronounced effects were concentrated on overlapping genomic locations (Fig. 3O), which suggests that in LA excitatory neurons, genomic regions particularly susceptible to epigenetic and transcriptional variability orbit around the functions of IE and synaptic transmission. In particular, the HAT mechanism of action reveals

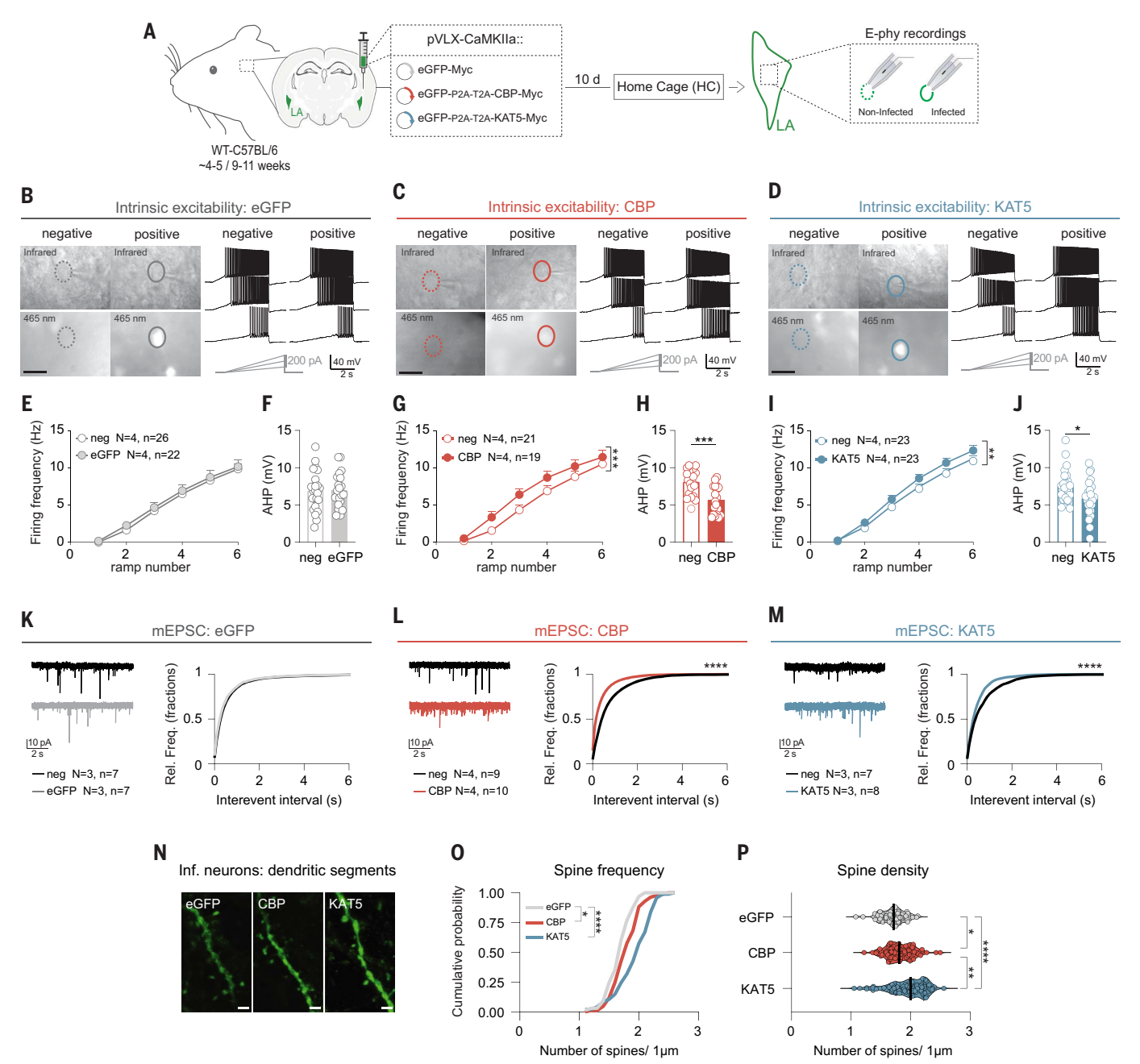


Fig. 4. HAT overexpression increases IE and synaptic functions. (**A**) Experimental design: The LA of WT mice was bilaterally injected with lentiviruses carrying eGFP, CBP or KAT5. After 10 days, brains were prepared for ex vivo patch clamp recordings or snMultiomics-sequencing. (**B** to **D**) Images (left panels) and neuronal firing traces (right panels) of eGFP-positive (B), CBP-positive (C) and KAT5-positive (D) neurons compared to nontransfected neurons (negative); scale bars: $20~\mu m$. (**E, G,** and **I**) Spike frequency in positive versus negative neurons in eGFP [two-way ANOVA, F (1, 276) = 1.335, P = 0.2489], CBP [two-way ANOVA, F (1, 228) = 11.54, P = 0.0008] and KAT5 [two-way ANOVA, F (1, 264) = 10.84, P = 0.0011] groups. (**F, H,** and **J**) After-hyperpolarizing potential (in mV) values in eGFP-, CBP-, or KAT5-infected animals. Asterisks represent the P-values of an unpaired t test with Welch's correction, between noninfected

and infected neurons. (**K** to **M**) mEPS recordings in pyramidal neurons and cumulative distributions of mEPSC intervent interval, indicating significantly higher mEPSC frequency in cells infected with CBP and KAT5. Significant difference between cumulative distributions was tested with the Kolomogorov-Smirnov test, with P-values < 0.01. (**N**) Images of eGFP-, CBP-, and KAT5 LA-infected neurons; eGFP is indicated in green. Scale bars are 2 μ m. (**O**) Percentile plot reporting the percentage of neurons with a given spine density. (**P**) Spine density distributions across eGFP-, CBP-, and KAT5-infected neurons; each circle is a neuronal dendritic segment. For (0 to P), n = 4 to 6 mice per group. Kruskal-Wallis test (P < 0.0001), followed by Dunn's multiple comparisons test between groups. For all tests: *, $P \le 0.05$; ***, $P \le 0.01$; ****, $P \le 0.001$; ****, $P \le 0.0001$.

the presence of the highly dynamic nature of chromatin accessibility (39) in post mitotic neurons, which can either guide a gene's priming (DA@TSS genes), reinforce its chromatin architecture (DA≠TSS genes) or enhance its transcription (DE genes) depending on the chromatin environment that the HATs encounter (fig. S9).

With such predisposition, a neuron's epigenetic landscape might represent an adaptive mechanism to register and integrate environmental signals in a dynamic yet long-lasting

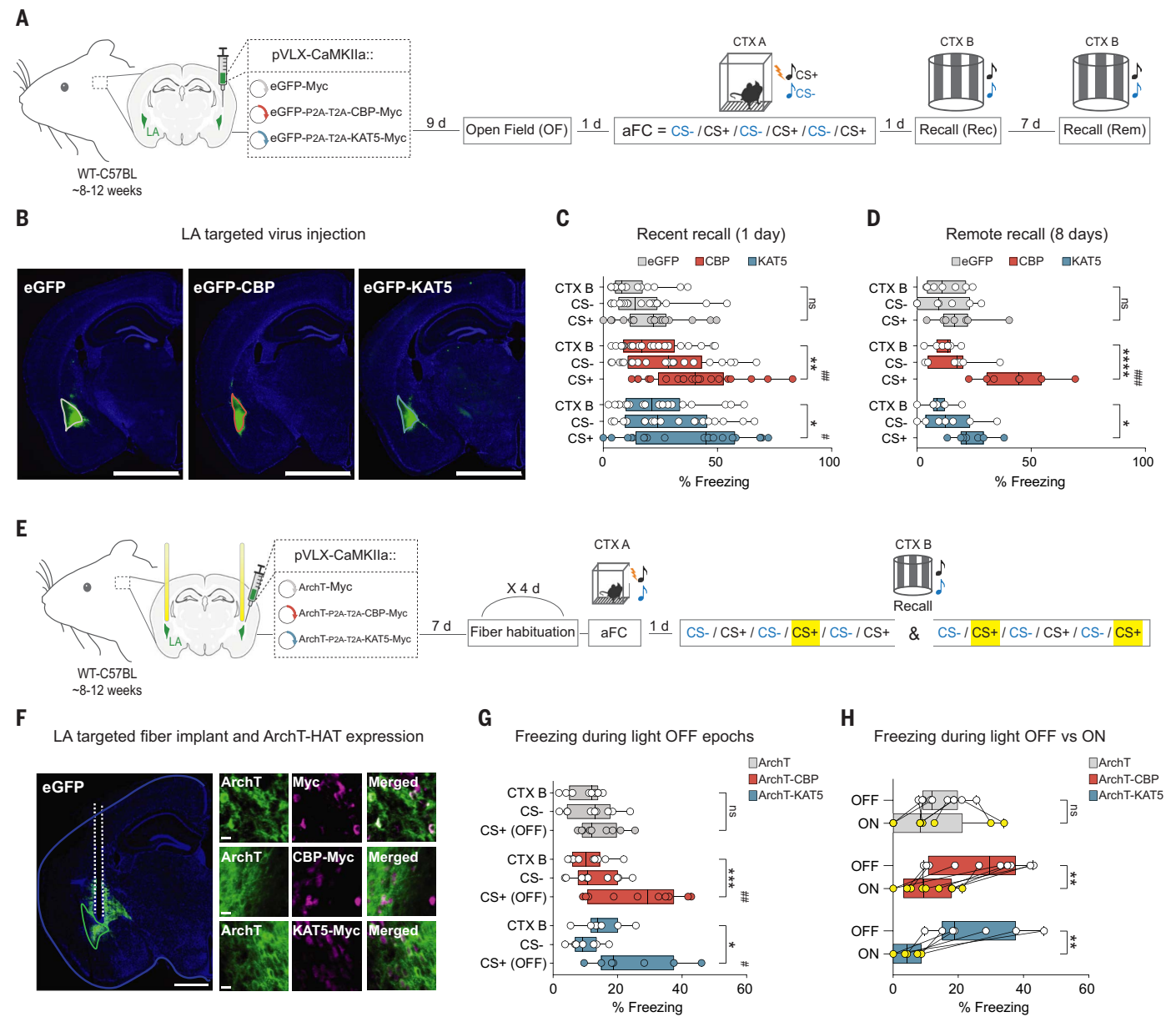


Fig. 5. HAT overexpression facilitates while optogenetic silencing of **HAT-infected neurons disrupts memory retention.** (A) Experimental design: The LA of adult WT mice was bilaterally injected with lentiviruses carrying eGFP, CBP, or KAT5. After nine days a subgroup of mice underwent open field testing. Following surgery (10 days after), mice were subjected to an aFC paradigm allowing for context discrimination. Following training (24 hours after). recent memory was tested (recall 1). One batch of mice was also tested for remote memory (recall 2) 8 days post encoding. CTX, context; CS+, conditioned stimulus; CS-, unconditioned stimulus. (B) Images of eGFP-, CBP-, and KAT5 LA-targeted injections; Hoechst (blue) and eGFP (green). Scale bars are 2 mm. (C and D) Freezing levels during recent (C) [two-way ANOVA, F (2, 168) = 10.43, P < 0.0001 and remote memory recall (D) [two-way ANOVA, F (2, 54) = 5.078, P = 0.0095] in eGFP, CBP, or KAT5 groups. Two-way ANOVA was followed by Holm-Šídák test, which allowed for intra-group comparison of changes in freezing levels in CTX B to CS+ (asterisks) as well as for intergroup comparisons at CS+ across conditions represented as hashtags. Each circle is an average value reported per mouse, n = 19 to 21 mice per group. (**E**) Experimental design for the optogenetic silencing of HAT-overexpressing neurons: The LA of

WT mice was bilaterally injected with lentiviruses either carrying ArchT alone, ArchT-CBP, or ArchT-KAT5. Optic fibers were implanted bilaterally above the LA. Prior to aFC mice were exposed to four days of patch cord habituation. One day after encoding, mice were tested for memory recall. Yellow bars highlight the time bins during which the 593-nm laser to activate ArchT was turned on. (F) (Left) ArchT expression in LA neurons and localization of the optical fiber implant. Scale bar is 1 mm. (Right) Enlarged view of LA neurons infected with ArchT (green) and Myc, or ArchT-HAT-Myc (purple). Scale bar is 20 μm. (G) Mean freezing levels during light OFF epochs [two-way ANOVA, F(2, 69) = 12.66, P < 0.0001 at recent recall. Two-way ANOVA was followed by Holm-Šídák test, which allowed for intra-group comparison of changes in freezing levels in CTX B to CS+ (asterisks) as well as for the intergroup comparisons at CS+ across conditions (hashtags). Each circle is an average value reported per mouse, n = 7 to 12 mice per group. (H) Mean freezing levels during light ON and light OFF CS+ epochs [two-way ANOVA, F (2, 46) = 3.255, P < 0.0489]. Asterisks represent the P-values of Šídák tests for the ON versus OFF comparison across the three conditions. For all tests: *, $P \le 0.05$; **, $P \le 0.01$; ***, $P \le 0.001$; ****, $P \le 0.0001$; ns, not significant.

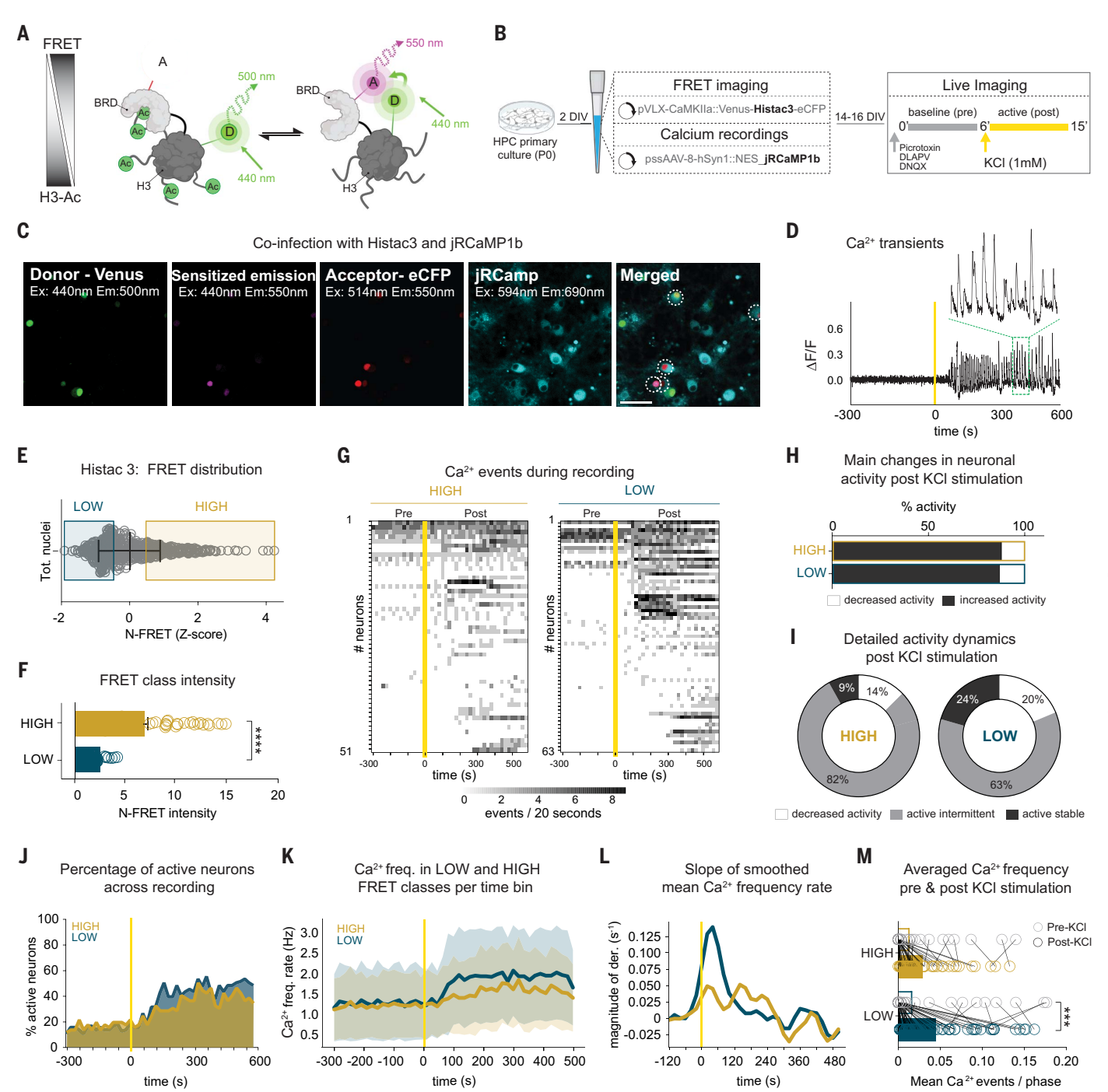


Fig. 6. Histone acetylation and IE are linked in a cell-autonomous manner at single cell resolution. (A) Schematic representation of the FRET probe's mechanism of action. (B) Experimental design: Hippocampal primary cultures (DIV 2) were coinfected with a lentivirus carrying the Histac3 FRET probe and an AAV delivering the RCamp1b calcium reporter. Two weeks later, neurons were imaged for sensitized emission and calcium activity before and after KCl stimulation. (C) Coinfection image of Venus-donor fluorophore (green), sensitized emission (purple), eCFP-acceptor (red), jRCamp (cyan); scale bar 20 μm . (D) Example of calcium transients' traces during recording and zoomedin illustration of peak detection. (E) Distribution of the z-scored FRET values of the neuronal population immediately before KCl application. Rectangles highlight the clusters of the low (blue) and high (yellow) class used for further analysis. Every circle is a nucleus. (F) Mean FRET intensity in HIGH versus LOW class neurons. Asterisks represent the *P*-values of an unpaired *t* test with

Welch's correction; each circle represents a nucleus. **(G)** Neuronal population activity dynamics pre and post KCl stimulation: No Ca^{2+} transients in white, Ca^{2+} transients in black gradient. **(H)** Percentage of neurons with increased mean Ca^{2+} transients post KCl (black) and decreased mean Ca^{2+} transients post KCl (white) compared to baseline. **(I)** Percentage of neurons with intermittent or stable activity pattern within increased Ca^{2+} frequency post-KCl population. **(J)** Percentage of active neurons per time bin throughout recording in HIGH and LOW FRET neuronal populations. **(K)** raw numbers of Ca^{2+} transients per time (Hz) throughout recording in HIGH and LOW recording in populations. **(L)** Slope of mean Ca^{2+} transients in HIGH and LOW neuronal populations. **(M)** Mean dynamics of Ca^{2+} events within each FRET class pre and post-KCl [two-way ANOVA, F (1,224) = 17.47, P < 0.0001]. Every circle is a nucleus and asterisks represent the P-values of Šídák tests comparing the Ca^{2+} freq. in HIGH and LOW classes pre versus post KCl. For all tests: *, P < 0.05; ***, P < 0.001; ****, P < 0.001; ****, P < 0.0001.

fashion, akin to the notion of a genomic action potential (40). How this epigenetic landscape in turn is influenced by other epigenetic marks, metabolic rates (41), or circadian rhythms (42), its precise timescales, and whether its dysregulation might lead to altered memory allocation in neurological disorders remains unknown. These open questions notwithstanding, the present findings show that epigenetic mechanisms—in addition to stably defining neuronal niche formation during development—are essential in predetermining higher-order neuronal functions.

Materials and Methods *Animals*

All animal work was performed in accordance with procedures and ethical guidelines approved by the EPFL and the Veterinary Office of the Federal Council of Switzerland, under the animal licenses VD3413 and VD3413.1. Switzerland's law on animal welfare places a lot of weight on the 3R principles, in particular the reduction of the use of animals, which is why only one sex was chosen. We decided on male mice so as to avoid possible confounding effects of the estrous cycle in females. All animals employed in this study were male C57BL/6JRj mice purchased from Janvier Labs. For in vitro experiments, primary hippocampal neuronal cultures were derived from P0 C57BL/6JRj wild-type (WT) mice. For ex vivo experiments C57BL/6JRj mice between 4 and 5 weeks of age were used, for in vivo experiments C57BL/6JRj mice between 8 and 12 weeks of age were used. For all behavioral studies, mice were delivered at 4 to 7 weeks of age and left to acclimatize for at least 1 week before the start of the experiments. Animals were housed in groups of 2 to 4 mice per cage. Cages were kept at 22 to 25°C/55% humidity on a 12-hours light/dark cycle (light on 7:00) and provided free access to water and food ad libitum. All mice work was carried out during daylight and behavioral tests were performed between 8.30 am and 13.00 p.m.

Cell culture

P0 pups' hippocampi were dissected and incubated with papain (20U/mL, Sigma Aldrich) for 30 min at 34°C. The tissue was mechanically triturated to obtain a single cell suspension. For immunocytochemistry experiments, neurons were added on 35-mm well plates (ref: 353001, Falcon®35mm, Corning) at a density of 0.5×10^6 cells/plate. For live imaging experiments, neurons were cultured onto the coverslip of an IBIDI μ -Dish (ref: 81158, Martinsried, IBIDI) at a density of 0.3×10^6 cells/dish. In both conditions, to guarantee the attachment of the neurons to the coverslips, cells were first plated in minimum essential medium (MEM, ref: 21090-022, Gibco),

10% horse serum (Gibco), 0.5 mM L-glutamine (ref: 25030-024, ThermoFisher), 0.36% glucose, 100 U/mL penicillin and 100 $\mu g/mL$ streptomycin (Pen Strep, ref: 15140-122, Gibco). After 3 hours, the medium was changed to Neurobasal medium (ref: 21103-049, Gibco) containing 1/50 volume of B27 (ref: 17504-044, Gibco), 0.5 mM glutamine, 100 U/mL penicillin and 100 $\mu g/mL$ streptomycin. Neurons were kept at 37°C in a humidified atmosphere of 5% CO2, and the medium was never changed during the duration of the experiments.

Constructs production

Most of the constructs used in this study were developed in house. In short, transgenes were amplified with high-fidelity Prime STAR Max DNA Polymerase (Takara) according to the manufacturer's instructions. Inserts were released by restriction enzymes, digested and ligated into a pCMV6 (Origene) or a modified pLVX-CamKIIa (Clontech Laboratories). All cloned plasmids were verified by Sanger sequencing.

Inserts were derived from the following plasmids/sequences:

- CBP → pRc/RSV-m CBP-HA (ref: 16701, Addgene)
- KAT5 \rightarrow pCMV6-KAT5-Myc-DKK (ref: MR223769, Origene)
- HDAC2 \rightarrow pENTR223.1-HDAC2 (ref: HsCD00080462, DNASU)
- Histac3 \rightarrow pcDNA3.1-Histac3-H3K9/K14 (ref: RDB14340, RIKEN BRC)
- Histac4 → pcDNA3.1-Histac4- H4K5/K8 (ref: RDB12840, RIKEN BRC)
- P2A-T2A sequence: gcaacaaacttctctctgctgaaacaagccggagatgtcgaagagaatcctggaccgtctagagagggcagaggaagtcttctaacatgcggtgacgtggaggagaatcccggccct
- Myc-Flag sequence: gagcagaaactcatctcagaagaggatctggcagcaaatgatatcctggattacaaggatgacgacgataaggtttaa
- \bullet shCBP \to pGFP-C-shLenti with 4 unique 29mer shCBP constructs in lentiviral GFP vector (ref: TL500422, Origene)
- shKAT5 → pGFP-C-shLenti with 4 unique 29mer shKAT5 constructs in lentiviral GFP vector (ref: TL512714, Origene)

For in vivo experiments we used a modified version of the following inserts:

- 1. To accommodate the CBP sequence in lentiviral vectors, only the region containing the CBP HAT-catalytic domain was kept (from 3559 to 5538 bp of the original insert). To ensure the nuclear localization of the construct, an NLS signal was added to the CBP N-terminal (NLS sequence: GACTACCCAGCTGCTAAGAGAGTTAAGCTTGACGGAGGATCAGGA).
- 2. In order to manipulate the murine HDAC2 enzyme we reduced the size of the original vector (from 283 to 1746 bp) to only maintain the *Mus musculus* HDAC2-coding sequence.

CBP and KAT5 DM constructs:

- 1. To abolish the activity of the CBP-HAT catalytic domain, four point mutations were introduced in the NLS-CBP insert specifically at the: 1510 (c \rightarrow a), 1511 (t \rightarrow a), 1513 (t \rightarrow c) and 1514 (g \rightarrow t) bp positions. These modifications allowed for the transformation of the Leu¹⁶⁹⁰-Cys¹⁶⁹¹ to Lys¹⁶⁹⁰-Leu¹⁶⁹¹, and proved to efficiently impair histone acetyltransferase (HAT) activity as demonstrated (43).
- 2. To disrupt the activity of the KAT5-HAT catalytic domain, three point mutations were introduced in the KAT5 insert specifically at the: 1129 (c \rightarrow g), 1140 (g \rightarrow a) and 1141 (c \rightarrow g) bp. These modifications allowed for the substitution of the Gln³⁷⁷-Gly³⁸⁰ to Glu³⁷⁷-Glu³⁸⁰, and proved to efficiently impair histone acetyltransferase (HAT) activities as demonstrated by (44).

Mutations were introduced using the QuikChange XL Site-Directed Mutagenesis Kit (ref: 200516, Agilent) following the manufacturer's instructions.

Summary of the plasmids produced in house:

- pCMV6::eGFP-Myc-Flag
- pCMV6::CBP-Myc-Flag
- pCMV6::KAT5-Myc-Flag
- $\bullet \ pVLX\text{-}CamKIIa::NLS\text{-}Venus\text{-}Histac4\text{-}ECFP$
- pVLX-CamKIIa::NLS-Venus-Histac3-ECFP
- pLVX-CamKIIa::eGFP-Myc-Flag
- pLVX-CamKIIa::NLS-CBP-Myc-Flag
- pLVX-CamKIIa::KAT5-Myc-Flag
- pLVX-CamKIIa::eGFP-P2A-T2A-Myc-Flag
- pLVX-CamKIIa::eGFP-P2A-T2A-NLS-CBP-Myc-Flag
- pLVX-CamKIIa::eGFP-P2A-T2A-NLS-KAT5-Myc-Flag
- pLVX-CamKIIa::eGFP-P2A-T2A-NLS-HDAC2-Myc-Flag
- pLVX-CamKIIa::eGFP-P2A-T2A-NLS-CBP-DM-Myc-Flag
- pLVX-CamKIIa::eGFP-P2A-T2A-NLS-shCBP-Mvc-Flag
- pLVX-CamKIIa::eGFP-P2A-T2A-NLS-shKAT5-Myc-Flag
- pLVX-CamKIIa::eGFP-P2A-T2A-NLS-KAT5-DM-Myc-Flag
- pLVX-CamKIIa::ArchT-P2A-T2A-Myc-Flag
- pLVX-CamKIIa::ArchT-P2A-T2A-NLS-CBP-Myc-Flag
- pLVX-CamKIIa::ArchT -P2A-T2A-NLS-KAT5-Myc-Flag
- pLVX-CamKIIa::ArchT-P2A-T2A-NLS-HDAC2-Myc-Flag

Lentivirus production

Lentiviral vectors were produced in house in HEK-293T cells (ATCC) through a third-generation packaging system by calcium phosphate transfection, using the following plasmids: pMD2.G (2.5 μ g), psPAX2 (7.5 μ g) and pLVX-CamKIIa containing any of the required inserts (10 μ g), quantities refer to a 10 cm petri dish (ref: 353003, Falcon). Four days later, the medium was collected and centrifuged at 19,000 r.p.m. for 90 min

at 4°C, in a SW32Ti ultracentrifuge. The pellet was resuspended in buffer containing 1X PBS pH 7.4 and 0.5% BSA to reach a concentration of 4000X virus stock. Viral titer was determined using the HIV-1 p24 antigen ELISA kit (Zeptometrix Corp).

In vitro neuronal culture preparation for WB

At DIV6, primary hippocampal neurons were infected with 1000ng with pLVX-CamKIIa:: eGFP-P2A-T2A-NLS-shCBP-Myc-Flag or pLVX-CamKIIa::eGFP-P2A-T2A-NLS-shKAT5-Myc-Flag. Neurons were kept in incubator until DIV14 when collected and mixed with Laemmli buffer. Equal amounts of protein (50 µg/lane) were separated by a 4 to 12% acrylamide gel and transferred onto nitrocellulose membranes (Amersham, GE Healthcare) O/N 30V. Ponceau S staining (Sigma-Aldrich) was used for monitoring protein loading and transference. Nonspecific binding was blocked by incubation in 5% nonfat milk in Tris-buffered saline (100 mM NaCl, 10 mM Tris, pH 7.4) containing 0.1% Tween (TTBS) for 1 hour at room temperature. Afterwards, membranes were incubated overnight at 4°C with different antibodies. For cell lysates, protein loading was also monitored by using a mouse monoclonal antibody against total H3. Membranes were then incubated for 1 hour in the appropriate horseradish peroxidase-conjugated secondary antibodies (211-032-171 or 115-035-003, 1:5,000; Jackson ImmunoResearch), and immunocomplexes were revealed by an enhanced chemiluminescence reagent (ECL Advance, Amersham Biosciences). Densitometric quantification was carried out with Fusion FX software (Vilber).

In vitro neuronal culture preparation for FRET – Calcium live imaging

At DIV2, primary hippocampal neurons were infected with 250 ng pVLX-Histac3 and 3500 MOI AAV-syn-RCamp. Neurons were kept in incubator until DIV 10-14 when images were acquired. Cultures were brought to an inverted Leica SP8 microscope maintained at 37°C in a humidified atmosphere of 5% CO2 for live FRET and Calcium imaging. Neurons were first treated with a cocktail of DNQX (40 µM in DMSO, abcam ref: ab120018), DL-APV (100 µM in water, abcam ref: ab120271), and picrotoxin (100 µM in DMSO), to block synaptic transmission and inhibitory activity and thus detect intrinsic excitability in principal neurons. Neurons were then treated with a second cocktail of KCL (1mM) to induce an increase in neuronal activity. Both cocktails were prepared in 200 μ l of neurobasal media aliquoted from the well before the start of any acquisition and were added directly on the well during the recording.

FRET—Calcium live imaging—parameters of acquisition

FRET, 4 channels were acquired in three scanning modalities. First: eCFP, the donor fluorophore (emission 450 to 500 nm) was simultaneously acquired with the sensitized emission (SE), FRET signal, (emission 525 to 550 nm) using a single 440 nm laser for excitation. Second: Venus, the acceptor fluorophore (emission 525 to 550 nm) was acquired while exciting with a 514 nm laser. Third: RCamP (emission 610 to 690 nm) channel was acquired while exciting with a 594 nm laser. The pixel size was set to 0.303 microns and the z position was chosen to focus on the greater number of nucleus in one field of view of 620 $\mu m \times$ 620 μm . For all sequences 25 water objective and HyD detector. Calcium imaging, continuous RCamP was acquired with the same Ex/Em setting, with a pixel size of 2.431 microns and with a frame rate of 4.55 fr/sec. Z-position was adjusted to focus on the cytosolic RCamP signal. All laser power and detector gain were chosen to limit as much as possible the number of saturated pixels, while retaining an acceptable image signal to noise ratio.

Calcium imaging analysis pipeline

Region of interest (ROI) characterization: All data files were processed with custom-written codes in Fiji IJ1 macro language and Python. Recordings were stack-registered using the StackReg plugin (45) to account for potential shift in the field of view resulting from the addition of drug cocktails to the sample. ROIs were detected using a CellPose2.0 (46) model trained in house, and manually corrected in the GUI when needed. Finally, ROIs were imported in FIJI and mean calcium intensity of each neuron was extracted using FIJI Multi Measure function and saved in an .csv extension file.

Peak detection and traces analysis: We accounted for changes in baseline calcium fluorescence over the whole recording length by modeling the basal calcium intensity (F0) as a fluctuating trace of the same size of F. The calcium intensity (F₀) was computed using a custommade Python script from the raw calcium trace (F) of each neuron. To optimize the peak detection, F0 traces have been smoothed by means of an algorithm inspired by the finite difference diffusion equation (47). The normalized trace

on Cascade [GitHub (48, 49)]. Only neurons that showed a robust peak detection (i.e., same peak number identified in both $\Delta F/F_0$ traces versus a smoothed trace) were kept for analysis. Calcium transient's frequency, was defined as the number of Ca²⁺ events in 20 s. intervals. Pre and Post KCL frequency were defined as the total number of calcium events in the total baseline and stimulated phases respectively. The stable active class was defined as a continuous increase in Ca²⁺ frequency for 60% of the total stimulated phase, traces that did not show an increase prolonged firing but showed an increased activity compared to baseline were assigned to the intermittent class. The slope measurement corresponds to smoothed mean Ca2+ frequencies traces computed for their derivative using NumPy function.

 $\Delta F/F_0$ was computed as $(F-F_0)/F_0$ and processed

for peak detection using a modified algorithm

FRET imaging analysis pipeline

To ensure an unbiased nuclei detection the sum of the three FRET channels was used (donor, acceptor and SE). Images were processed on FIJI using Image Calculator built-in plugin, and transferred to QuPath 0.3.2 for nucleus detection and classification using a custom-made and trained classification algorithm (50, 51). Resulting ROIs were then manually corrected in FIJI and reclassified if necessary. Each ROIs was then extracted as a separate image using a FIJI custom made plug-in. FRET value was computed pixel-by-pixel using the following equation:

Normalized (Pixel) =
$$\underbrace{\mathit{ISE} - (\mathit{ID} * \mathit{BtD}) - (\mathit{IA} * \mathit{BtA}) - (\mathit{IRCamp} * \mathit{BtRCamp})}_{\mathit{IA}}$$

 I_{SE} : pixel intensity in the FRET channel, I_{D} : pixel intensity in the donor channel, IA: pixel intensity in the acceptor channel, I_{RCamp} : pixel intensity in the RCamp channel, Bt_D: signal bleed-through (SBT) of the donor in the SE channel, Bt_A: SBT of the acceptor in the SE channel, Bt_{RCamp} : SBT of the RCamp in the SE channel. SBT for each channel were measured in independent experiments where neurons were expressing either single fluorophores (donor or acceptor), or RCamP only; the extracted SBT values are considered constant and therefore used as such. We normalized by the IA to account for nuclear protein content and allow for internucleus comparisons. N-FRET was not computed for pixels reaching saturation in at least one of the channels. ROIs of nuclei showing saturation in more than 10% of their pixel were excluded from the analysis. The final nuclear N-FRET value corresponded to the mean N-FRET (pixel) computed for each of the pixels composing each nuclear ROI. For each of the three biological replicates, the distribution of N-FRET values was z-scored and based on their Z-N-FRET value nuclei were assigned to a class (LOW MID HIGH).

On each z-scored distribution, the mean and the standard deviation were computed and the

Secondary Ab (1:5000, ImmunoResearch)

H3 - Ms - (active motif 39064) - 1:2000 H3K27Ac - Ms - (active motif 39085) - 1:1000 CBP - Ms - (Santa Cruz sc7300) - 1:400 KAT5 - Rb - (Invitrogen PA5-23290) - 1:1000

Primary antibody

Horseradish-peroxidase (HRP)-conjugated goat-anti-mouse

(HRP)-conjugated mouse-anti-rabbit

classes defined as: $HIGH-LOW\ classses=mean\pm\frac{sd}{2}$ Nuclei showing intermediate value were assigned to the MID class.

Surgeries for viral injections and optic fiber implantation

For patch clamp experiments mice underwent surgery at 4 weeks of age. For all other behavioral experiments, surgical procedures were performed when animals were 8 weeks old. Mice were anesthetized by intraperitoneal injection of a mix of fentanyl (0.05 mg/kg, Sintetica), midazolam (5 mg/kg, Actavis), and metedomidin (0.5 mg/kg, Orion Pharma). Once deeply anesthetized, the head was shaved around the surgery site and subcutaneously injected with a local anesthetic mix containing lidocaine (6 mg/kg, Streuli Pharma) and bupivacaine (2.5 mg/kg, Sintetica), eyes were hydrated using viscotears (Carbomerum980 2 mg/g, Bausch+Lomb). The skin was opened with scissors and, once placed on stereotaxic frame, the skull was exposed and cleaned. Head orientation was adjusted to align bregma, lambda and medio-lateral references, with a 0.5 mm drill bit, holes were drilled bilaterally to reach the lateral amygdala coordinates (AP -1.12; ML ± 3.43 ; DV -4.48). After drilling, the skull was thoroughly washed with saline solution to avoid any debris to cause inflammation. The virus was injected at a speed of 100 nL/min, using pulled glass capillaries (intraMARK, Blaubrand, tip diameter 10-20 µm) connected to a syringe and a stereotaxic micromanipulator (Kopf Instruments). To reduce backflow the needle was left in place for 10 min before slow pull up. Capillaries were always changed between surgeries.

For the optogenetic experiment, two 200- μ m optic fibers (0.39 NA, Thorlabs) were implanted bilaterally 150 μ m above the LA injection sites (AP -1.1; ML \pm 3.4; DV -4.33).

At the end of the procedure, the skin was sutured (5/0 Prolene, Ethicon), and to reverse the anesthesia, animals were injected i.p. with atipamezol (2.5 mg/kg, Orion Pharma) and kept in a cage on a heating pad for at least 1 hour. Mice were administered paracetamol (Dafalgan, 1 mg/mL) in drinking water for a week.

All virus concentrations were adjusted with a dilution buffer (1X PBS pH 7.4 and 0.5% BSA) to reach the desired concentration of 450 ng/0.4 μ l of viral particles per site of injection. Animals were randomly assigned to different experimental conditions, and to account for behavioral variability between cages, the three experimental groups were always represented in every cage.

Mice for which the viral targeting of neighboring regions (such as Caudoputamen and Central Amygdala) was higher than 20% (irrespective of LA infection rates) were excluded from the analysis, as well as mice for which the infection of the neighboring regions was higher than the LA infection.

Ex vivo electrophysiology

Acute brain slices were prepared 10 days after

viral injection. Mice were anaesthetized with

isoflurane and decapitated. The brain was

quickly removed, and 250-µm thick coronal

slices containing the amygdala were cut with a vibrating tissue slicer (Campden Instruments) in oxygenated (95% O₂ / 5% CO₂) ice-cold modified artificial CSF (ACSF), containing (in mM): 105 sucrose, 65 NaCl, 25 NaHCO₃, 2.5 KCl, 1.25 NaH₂PO₄, 7 MgCl₂, 0.5 CaCl₂, 25 glucose, 1.7 L(+)- ascorbic acid. After cutting, slices recovered for 1 hour at 35°C in standard ACSF containing (in mM): 131 NaCl, 26 NaHCO₃, 2.5 KCl, 1.25 NaH₂PO₄, 1.2 MgCl₂, 2 CaCl₂, 18 glucose, 1.7 L(+)-ascorbic acid, and complemented with 2 sodium pyruvate and 3 myoinositol. For the evaluation of intrinsic excitability, in the recording chamber, slices were superfused with oxygenated standard ACSF at nearlyphysiological temperature (30 to 32°C). eGFPpositive neurons were identified through LED excitation (465 nm) and imaged with a RoleraTM Bolt Scientific CMOS camera (QImaging). Whole-cell patch clamp recordings were performed from pyramidal neurons in the lateral amygdala using borosilicate pipettes (3-4 MΩ) filled with (in mM): 130 KGluconate, 10 KCl, 10 HEPES, 10 phosphocreatine, 0.2 EGTA, 4 Mg-ATP, 0.2 Na-GTP (290-300 mOsm, pH 7.2 to 7.3). Recordings of miniature postsynaptic currents (mEPSCs) were conducted at room temperature in the presence of 0.01 mM tetrodotoxin and 0.1 mM picrotoxin, using borosilicate pipettes (2 to $3 \text{ M}\Omega$) filled with (in mM): 127 CsGluconate, 10 CsCl, 10 HEPES, 10 phosphocreatine, 0.2 EGTA, 4 Mg-ATP (290-300 mOsm, pH 7.2 to 7.3). Liquid junction potential was not corrected for. eGFP-positive neurons were identified through LED excitation (465 nm) and imaged with a RoleraTM Bolt Scientific CMOS camera (QImaging). Input resistance was assessed by the passive current response to a hyperpolarizing step of -10 mV while cells were held at -60 mV. Putative pyramidal cells were first visually identified based on the pyramidal shape of the cell body. We further excluded neurons (n = 7) with low capacitance (<50 pF) and high input resistance (>500 MOhm), as these values are indicative of GABAergic interneurons (52-54). Resting membrane potential was measured within the first 2 min whole-cell establishment with no current injection. Current-clamp recordings were conducted using bridge compensation. To elicit neuronal firing, cells were held at -60 mV with direct current injections, and somatic current injections of increasing amplitude were provided using ramps of 5 s (6 ramps with final amplitude ranging from 50 pA to 300 pA). Rheobase and the firing threshold were measured as the level of current and voltage, respectively, that induced the first action potential in the ramp protocol. For after-hyperpolarizing potential (AHP) measurement, square depolarizations were provided instead of ramps, and the first generated action potential was considered. Recordings of mEPSCs were conducted for 5 min in cells were held at -60 mV. Signals were acquired through a Digidata1550A digitizer, amplified through a Multiclamp 700B amplifier, sampled at 20 kHz and filtered at 10 kHz using Clampex10 (Molecular Devices). Analyses of intrinsic excitability were conducted in Clampfit10 (Molecular Devices). For detection of mEPSCs, traces were filtered at 1 kHz and analyzed with Easy Electrophysiology v2.3 (Easy Electrophysiology Ltd., UK) using the template detection method with an amplitude threshold of 4.5 pA. Detected events were verified by visual inspection. To construct cumulative frequency plots, the first 200 events recorded in each cell were considered.

Auditory fear conditioning

For all behavioral experiments:

Mice underwent cued auditory fear conditioning (MultiConditioning System, TSE systems) 10 days after surgeries. Freezing was automatically measured when absence of movement was detected for more than 1 s using an infrared beam capture system. Freezing was calculated as the average time spent freezing across 10 s bins of time. To account for any effect induced by transportation to the behavioral spaces, home cage control animals underwent the same displacements but were not exposed to any handling, tests, or new environment before being sacrificed.

• For the LA endogenous epigenetic characterization and allocation studies:

On the day of aFC, animals were placed in the dedicated conditioning chamber (CTX A: squared, with grid floor and transparent walls) for an exploratory phase of 2 min. Next, an auditory conditioned stimulus (CS+: 2800 Hz, 85 dB) was presented for 30 s and paired with a mild foot shock (US: 0.2 mA) during the last two seconds of tone exposure. The session ended after an additional 30 s, and mice were brought back to their home cage. One hour after conditioning mice were sacrificed.

Only in the context of Fig. 1, to ensure that the mild aFC paradigm that we used in all subsequent experiments, in which we studied memory allocation, indeed triggered a significant increase in memory retention, we included a context-only control group (not used any further). Mice who received the mild shock were compared to mice that were exposed to the tone but never received the shock (context-only group).

· For immediate shock deficit studies:

On the day of aFC, animals were placed in the dedicated conditioning chamber (CTX A: squared, with grid floor and transparent walls) and immediately thereafter exposed to a mild foot shock (US: 0.2 mA, 2 s). Mice were left in CTX A for an exploratory phase of 1 min, followed by the presentation of an auditory conditioned stimulus (CS: 2800 Hz, 85 dB, 30 s). The session ended after an additional 30 s, and mice were brought back to their home cage. For the LA endogenous epigenetic characterization study (fig. S2, C and D) mice were sacrificed one hour after conditioning. For all other immediate shock deficit studies, a recent recall was performed one day after encoding in a modified chamber (CTX B: rounded, smooth floor, striped pattern walls and vanilla sent). The exploratory phase of 2 min was followed by the presentation of the CS+ for 1 min.

· For recent and remote recall studies:

On the day of aFC, animals were placed in the CTX A for an exploratory phase of 2 min. Subsequently, mice were exposed to an alternated sequence of two different tones each lasting 10 s and spaced with an inter trial interval (ITI) of 15 s. The neutral tone CS-(10000 Hz, 85 dB, 10 s) was never paired to the US, whereas every CS+ (2800 Hz, 85 dB, 10 s) delivery co-terminated with a mild foot shock (0.2 mA, 2 s). The sequence was presented three times. Recent recall was tested one day after encoding in a modified chamber (CTX B: rounded, smooth floor, striped pattern walls and vanilla sent). The exploratory phase of 2 min was followed by the six presentations of the two auditory stimuli: CS+ and CS- (10 s each, ITI 15 s). For the remote recall, a subgroup of mice returned to the CTX B seven days after the recent recall and underwent the same recall protocol.

• For the optogenetic experiment:

Seven days after surgery, for four consecutive days, each mouse was connected to the patch cord (200-µm diameter and 0.22 NA, Doric Lenses) for three minutes of free exploration of a clean housing cage. aFC was conducted as described above, and even when no light stimulation was delivered, mice were connected to the patch cord. On the following day, mice were plugged to the patch cord, placed in CTX B and memory recall was tested. During the second CS+ presentation, a yellow light was continuously delivered for 10s from a 593-nm laser (optogenetic inhibition). On the next day, mice were exposed to the same protocol although optogenetic inhibition was delivered during the first CS+ and third CS+ presentation. Before the start of every recall session the light power at the fiber tip was measured and calibrated at around 8 mW.

Mice were sacrificed on the same or following day of the last recall for injection site and fiber implant verification.

Open field test

To measure baseline anxiety, exploration, and locomotion behavior, nine days after surgery, mice were placed in a circular arena (72 \times

72 cm) for 10 min. Mice video tracking, quantification of the time spent in the arena (center, periphery, intermediate zones), as well as, animals' velocity and total distance moved, was performed with the EthoVision XT system (Noldus). After the test, mice returned to their home cages.

Immunohistochemistry and image acquisition

For all histological studies, animals were anesthetized with pentobarbital (150 mg/kg, Streuli Pharma) and perfused transcardially with 1× PBS for 1 min followed by 5 min of paraformaldehyde (4% PFA, 1 PBS, pH 7.4). Once extracted, the brains were post-fixed overnight in 4% PFA. Samples were transferred in cryoprotectant (30% sucrose, 1× PBS, 4°C, 48 hours) and frozen in cryomatrix at –80°C. 20 μm thick coronal sections were cut using a sliding cryostat (Leica Microsystems) and kept free-floating in antifreeze solution (30% ethylene glycol, 15% sucrose, 0.02% azide in 1× PBS) until staining.

Sections were washed in 1× PBS 3 times for 10 min each, blocked (1% BSA, 0.3% Triton-X in 1× PBS) for 90 min at RT, and incubated with primary antibodies overnight at 4°C in antibody dilution buffer (1% BSA, 0.1% Triton-X in 1× PBS). Slices were washed in 1× PBS + 0.1% Triton-X, and then incubated with fluorescently conjugated secondary antibody for 2 hours at RT under constant shaking. After three washes of 10 min in phosphate buffer 0.1 M, slices were stained for 5 min at RT with Hoechst 33342 (1:2500 dilution, in 1× PBS, Life Technologies) and washed three times before being mounted on glass slides using Fluoromount-G mounting medium (Southern Biotech). Slides were kept in the dark at 4°C until image acquisition. A total of five sections per animal was used. To span across the antero-posterior dimension of the LA one slice every 4 was taken. Images were acquired using a Zeiss LSM700 laser scanning confocal microscope using a 20× objective. Settings for the acquisition of HP1, H3K27Ac, cFos and Hoechst signals were kept identical across samples. To compare intensities across sections the beginning and the end of the specimen was

measured and only the Z-stack found in the middle position was acquired.

For H3K27Ac-Myc/eGFP analysis a total of three sections per animal was used spanning from the start to the end of the infected area (identified prior staining with the EVOS FL digital microscope, Thermo Fisher Scientific). Settings for the acquisition of H3K27Ac and Hoechst signals were kept identical across samples, while Myc-488/eGFP signals were adjusted to best detect either eGFP, CBP, or KAT5 infected neurons.

For cFos-Myc allocation study a total of five sections per animal was used spanning from the start to the end of the infected area (identified prior staining with the EVOS FL digital microscope, Thermo Fisher Scientific). Images were acquired using Olympus slide scanner VS120 L100 with a 20× objective. Settings for the acquisition of Hoechst and CY5 (cFos) signals were kept identical across samples, while FITC (Myc/eGFP) signals were adjusted to best detect either eGFP, CBP or KAT5 infected neurons

For spine density quantifications, images were acquired on a LCS SP8 confocal microscope (Leica). LA eGFP positive neurons were first identified under low magnification (×20), and dendritic segments subsequently under higher magnification (×40, zstack, 0.5 voxel size, zoom factor 1). Neurons showing intact dendrites in each region were selected. For the quantification of dendritic spines in the selected region, sections were imaged under a high magnification (x63, z stack, 0.4 voxel size, zoom factor 2). A stack of sequential images was generated. This ensured the accurate reconstruction of entire dendritic segments, and enabled counting of the segments with all visible spines on three-dimensional images.

For injection site and optic fiber implant validation, a total of three sections per animal was used spanning from the start to the end of the infected area (identified prior staining with the EVOS FL digital microscope, Thermo Fisher Scientific). Images were acquired using Olympus slide scanner VS120 L100 with a 20× objective.

Primary antibody	Secondary antibody (1:800, Invitrogen)
HP1 – Rb – (Invitrogen PA5-28488) – 1:1000	Alexa Fluor 488 donkey anti-rabbit IgG
CamKlla: Ms (Cayman 1E+07) - 1:600	Alexa Fluor 568 donkey anti-mouse IgG
H3K27Ac - Rb (ab4729) - 1:1800	Alexa Fluor 488 donkey anti-rabbit IgG
H3K27Ac - Ms (Active Motif 39685) - 1:2000	Alexa Fluor 568 donkey anti-mouse IgG
H4K5Ac Ms (Active Motif 61523) - 1:1000	Alexa Fluor 568 donkey anti-mouse IgG
cFos - Gp (sysy 226308) - 1:4000	Alexa Fluor 647 donkey anti-guinea pig lg(
cFos - Rb (sysy 226003) - 1:2500	Alexa Fluor 647 donkey anti-rabbit IgG
Myc - Rb (ab9106) - 1:1500	Alexa Fluor 488 donkey anti-rabbit IgG
Flag – Ms (sigma F1804) – 1:1000	Alexa Fluor 488 donkey anti-mouse IgG

Image analysis

For all in vivo experiments, images were analyzed with QuPath v0.2.1, v0.2.3, v0.4.3. A deeplearning-based method, StarDist (51), was trained to specifically detect Hoechst positive LA nuclei with high fidelity. The nuclear features and Hoechst values of CaMKIIa positive neurons were used to build a "CaMKIIa+" object classifier (50) to only compare nuclei with similar parameters across all the experiments, where for technical reasons it was impossible to add a neuronal marker. The specificity of the antibody was confirmed by dividing each nuclear signal by its cytosolic corresponding values and assessing that, for nuclear markers such as HP1, H3K27Ac, cFos and Hoechst, the ratio was > 1, while for cytosolic markers such as CamKIIa, the ratio was <1. Both percentages of cFos positive (ensemble size) and eGFP positive (infection rate) nuclei were related to the total amount of neuronal cells (tot. Hoechst).

For HP1 and H3K27Ac studies, for each acquired channels, the area and the intensity parameters of nuclear and cytosolic annotations were exported. Briefly, only nuclei that passed the CaMKIIa exclusion criteria were further analyzed. To account of variability across sections, nuclear HP1 and H3K27Ac intensities were normalized by their Hoechst corresponding value. Only nuclei that expressed a cFos intensity > 20 were classified as cFos positive. To build H3K27Ac classes, the mean nuclear intensity and standard deviation (SD) values were measured for all neuronal nuclei, in each animal separately. Nuclei expressing H3K27Ac levels lower than the mean - (SD/1.2) were classified as low H3K27Ac, whereas nuclei with H3K27Ac levels higher than the mean + (SD/1.2) where assigned to the high H3K27Ac class. All values in between belonged to the medium class. To highlight differences in classes enrichment between cFos positive and negative nuclei the percentage of occupancy of each class was calculated (% H - M or L / total H3K27Ac nuclei) and the ratio between positive and negative was reported. When measuring the enrichment in H3K27Ac levels in HAT-overexpressing studies, the percentage of occupancy of each class was calculated (% H -M or L / total H3K27Ac nuclei) and the ratio between infected versus noninfected neurons was reported. In these experiments reported mice values were averaged across sections.

For cFos allocation studies and infection site validations, the LA regions were manually outlined following the Allen Brain Reference Atlas superimposed onto the Hoechst signal. Only mice with and infection rate higher than 2% where kept in the study. eGFP and cFos colocalization analysis where based on the nuclei classification assigned by a custom-built script based on threshold intensities. cFos allocation was calculated as (cFos+ and eGFP+

nuclei) / tot. cFos nuclei. Chance ratios were calculated as (cFos+ and eGFP+ nuclei/ tot. Hoechst) / chance level, where chance level was the measured as follows: (cFos+/ tot. Hoechst) \times (eGFP+/ tot. Hoechst).

Finally, the distribution analysis ("binning") allowed us to measure the relative frequency of nuclei carrying a certain level of the screened epigenetic marks. For that, we ranked the spectrum of intensity values of the epigenetic marks in "intensity bins", where each bin contains the percentage of nuclei that lie within the range of values that define the bin [as also done elsewhere for epigenetic markers (55)].

For the quantification of dendritic spines, images were analyzed with ImageJ (version 2.1.0, National Institutes of Health), using the Cell Counter plugin. All measurements were performed by an experimenter blind to the experimental conditions. EGFP staining was used to assess changes in neuronal morphology of infected neurons. Spine density was measured on 3 neurons per slice. For each neuron, at least 3 dendritic segments were analyzed and spines were counted manually across the z-stack. At least 20 fragments per group were quantified.

LA isolation, nuclear extraction, and multiomic sequencing

For every experimental condition, both LAs of 3 mice were pooled. Ten days after surgeries, mice were sacrificed by cervical dislocation, their brain extracted, rinsed in 1× PBS at 4°C, placed in an ice-cold brain mold and coronally sliced (100 um per slice). Slices containing the amygdala were placed in a dish containing 1× PBS at 4°C. Under magnifier lenses the LA was manually isolated, collected and immediately frozen on dry ice. Frozen tissue was homogenized in 100 µL homogenization buffer NP+ (250 mM sucrose, 25 mM KCl, 5 mM MgCl2, 10 mM Tris·HCl, pH 7.4; plus 1 mM DTT, 1× protease inhibitor 50×, 1 U/uL RiboLock RNAse inhibitor, 0.1% NP-40, in H20), filtered through a 40 μm cell strainer and washed with 500 μL homogenization buffer (no NP-40). Samples were centrifuged at 1000 g for 8 min at 4°C. The pellet was resuspended in 210 µL homogenization buffer (no NP-40), and 290 µL of 50% Iodixanol solution (Iodixanol 60%, IDM 1×, 1 mM DTT, 1× protease inhibitor 50×, 1 U/uL RiboLock RNAse inhibitor) was added. Nuclei suspension was transferred to a tube (ref:344090, Beckman), completed with a layer of 100 µL homogenization buffer (no NP-40) and centrifuged at 10000 g for 22 min at 4°C using SW 55 Ti rotor, Optima XL-80K ultracentrifuge (56). Pellet was resuspended in 100 μ L of permeabilization buffer (250 mM sucrose, 25 mM KCl, 5 mM MgCl2, 10 mM Tris-HCl, pH 7.4; plus 1 mM DTT, 1× protease inhibitor 50×, 1 U/uL RiboLock RNAse inhibitor, 0,01% Tween, 0,001% Digitonin, 0,01% NP-40, 0,5% BSA, in H20) for 2 min at 4°C, 500 µL of wash buffer (250 mM sucrose, 25 mM KCl, 5 mM MgCl2, 10 mM Tris·HCl, pH 7.4; plus 1 mM DTT, 1× protease inhibitor 50×, 1 U/uL RiboLock RNAse inhibitor, 0,5% BSA, in H20) were added and samples were centrifuged at 1000 g for 10 min at 4°C. Pellets were resuspended in diluted nuclei buffer (see Chromium nuclei isolation kit, 10× Genomics) and filtered through a 40 µm Flowmi strainer. Final sample concentrations were eGFP: 4040 nuclei/uL, CBP: 3645 nuclei/uL, KAT5: 2925 nuclei/uL. Samples were immediately processed for Chromium Next GEM Single Cell Multiome ATAC + Gene Expression sequencing by the Gene Expression Core Facility (GECF, EPFL).

Single cell 10× multiome sequencing analysis (GEO accession GSE220696, security token: ubuhemeqbjalxyh.)

snRNA-seq and snATAC-seq libraries were processed with CellRanger-arc software (v. 2.0.0) using a custom mouse reference genome built from the mm10 genome and combined with the pVLX lentiviral vector carrying either eGFP, CBP, KAT5, both having the shared CamKII sequence masked (Cellranger). Cells with at least one ATAC-seq or RNA-seq read mapping to the lentiviral vector were labeled as infected cells. Downstream analysis was performed with R (v. 4.0.0) using in-house R-scripts and R packages Seurat [v4.1.0 (57)] and Signac (58), following the standard workflows with default settings unless specified. The processing of the individual samples consisted in selecting cells with expected RNA or ATAC counts (between 1K and 25K for RNA, and between 1K and 100K for ATAC) and a good quality ATAC signal defined by a nucleosome signal less than 2 and TSS enrichment greater than 1.

Individual eGFP, CBP and KAT5 RNA datasets were combined into a single Seurat object by using the following steps: Seurat Canonical Correlation Analysis by successively running SelectIntegrationFeatures, gene selection (3000) to base the integration on, FindIntegrationAnchors using CCA dimensions 1-30 and, finally, IntegrateData. Cells contained in this integrated object (total of 12'642 cells, derived from our three libraries eGFP (4445 cells), CBP (4449 cells) and KAT5 (3748) were further grouped into 18 clusters (FindClusters at a resolution of 0.4 using the integrated assay (see table S1), and manually associated to one of the following cell-type Astrocytes, Microglia, Oligodendrocytes, OP or Neurons, based on the RNA expression of some known markers (see table S2). Next, neuronal cells only were further classified based on a set of LA-specific and nonLAspecific transcripts (see table S3) refined from published data (59), associating each of the 22 clusters obtained on the Seurat object by running FindCluster with a resolution of 0.4 (see tables S1). To support this regional clustering

an additional regional score was calculated for each set of genes using the R package UCell v1.3.1 (60) (AddModuleScore UCell). Ambiguous cells were removed from the LA clusters. LA neuronal cells were further split into excitatory (Exc.) and inhibitory (Inh.) neuronal subtypes using individual expression profiles of marker genes refined from recently published datasets (61), as well as a UCell score to refine the labeling 4 (see tables S1, S4). This final set of 3491 LA excitatory neuronal cells was further characterized into 12 excitatory sub-clusters (Seurat FindAllMarker and FindCluster with a resolution of 0.4, 4 (see table S1) and topmarkers were identified based on the subset of cells composing each of them (fig S6 C).

Both integrated RNA-seq and ATAC-seq assays were merged to form a joint and unique multimodal Seurat object containing the LA excitatory neurons following the merging workflow described here (62). Briefly, we created a unified set of peaks [merging overlapping peaks with reduce method of the R package GenomicRanges (v. 1.40.0)] from the peaks derived from each condition (Signac function CallPeaks and macs3 (63), and removed nonstandard chromosomes and peaks found in blacklist regions (Signac functions keepStandardChromosomes and subsetBy-Overlaps). Next, a new feature matrix and chromatin assay was built (FeatureMatrix and CreateChromatineAssay) and processed following the standard Signac recommendations (normalization and identification of variable features using RunTFID and FindTopFeatures using all features). An additional joint UMAP was produced by using the Seurat weighted shared neighbor method (wsnn), which generates a joint neighbor graph considering both modalities (FindMultiModalNeighbors using the first 50 PCA component for the RNA-seq and 2:50 first lsi components for the ATACseq, followed by RunUMAP setting nn.name to weighted.nn).

LA excitatory neurons were classified as "active" based on the expression levels of cFos and of the class of rapid immediate early genes classified in Tyssoswky et al. study (24). In particular, an activity score calculated as the 90th percentile of cFos mRNA, and top 5 most expressed rIEGs. Neurons were considered as active cells when this score was above a threshold of 1. The most frequently expressed top genes among our cells were Nr4a1, Egr1, Egr3, Npas4, Junb, Arc, Btg2, Fos. Moreover, we calculated a cell accessibility score for different sets of genes, defined as the average ATAC signal observed in the gene body, extended to 2kb upstream (obtained by the method GeneActivity of Signac package).

We divided our datasets based on infection and neuronal activity states: eGFP control did not show any difference in the expression of the neuronal activity markers in infected ver-

sus noninfected neurons, therefore, was classified eGFP excitatory neurons only based on the neuronal activity label. We obtained a total of 10 groups (2 for eGFP - active or inactive; 4 groups for CBP - inactive noninfected, inactive infected, active non infected and active infected, and the same for KAT5). In order to find specific transcriptional signatures characterizing these groups, first we run individual differential expression analysis for each condition eGFP, CBP and KAT5 (FindAllMarkers, down sampling each identity class to 1000 cells), then we compared these 10 groups focusing on the average expressions profiles of up-regulated genes (adjusted P-value < 0.05) using a Spearman correlation plot (ComplexHeatmap package), a hierarchical clustering, as well as with a multidimensional scaling analysis (mdscale function from R package stats (v.4.3.0).

A new set of peaks was called for the infected excitatory neuronal cells following the same procedure as for the excitatory neuronal cells. Peaks were further annotated with annotatePeak [R package ChIPseeker (v1.24.0) (64)], using library TxDb.Mmusculus.UCSC. mm10.knownGene, defining the TSS region to [-1000, 1000] and keeping the default genomic annotation priority (that is with the following order Promoter, 5'UTR, 3'UTR, Exon, Intron, Downstream & Distal). We further defined a new category named "Promoter Extended" (PromExt) regrouping peaks annotated to Promoter, 1st Intron, 1st Exon and 5'UTR.

Differentially accessible regions (DAR) in HAT infected excitatory neuronal cells compared to eGFP infected cells were identified by comparing the ATAC signals in CBP (or KAT5) to the control eGFP, for each peak found in the aforementioned unified peak set (using Seurat method FindMarkers with LR test and using nCount peaks as latent variables). Peaks with a P-value < 0.01 and an absolute log fold-change > 0.25 were considered as significant (see tables S5, S6). Differential Expression (DE) analysis in HAT infected excitatory neuronal compared to the eGFP infected cells was done using the Seurat method FindMarkers on the integrated Seurat object reduced to the infected cells only (by applying an LR test, down sampling to the minimum number of cells in eGFP, i.e., 65 cells, and by removing the default minimum detection rate and log fold-change constraints). Genes with a *P*-value \leq 0.05 and an absolute log2 fold-change greater or equal to 0.5 were considered as being significantly up- or downregulated (see tables S7, S8). Functional enrichment analyses were done using compareCluster from R package clusterProfiler [v.3.16.1 (65)], referring to the Mouse library org.Mm.eg.db (v3.11.4). A P-value cutoff of 0.05 was used to define the significance of the enrichment. To quantify the amount of DA peaks with H3K27Ac, we considered the Naïve hippocampal CA1 H3K27Ac ChIP-seq datasets (GEO GSM1939151 and GSM1939152) published in (18), and ran a narrow peak calling with macs3 (63) from the combined replicates, with the following parameters: -c 10 -l 300 -g 1000. We then reported the overlap with FindOverlap from the R GenomicRanges package (v1.54.1).

Individual ATAC signal tracks were generated from infected neuronal cells adapting the Signac method ExportGroupBW from a more recent version of Signac (66), defining the tile sizes to 50bp, and normalizing the number of fragments per tile to the number of cells. Heatmaps showing the ATAC signal distributions around the TSS or around the middle of the peaks (in the peak-centric plots) were done with the R package EnrichedHeatmap (v1.29.3), running the method EnrichedHeatmap from matrices prepared using normalizeToMatrix with the following parameters [value_column = "score", mean mode = "weighted", extend = 1000, w = 50, background = 0, smooth = TRUE, keep = c(0,0.99)]. DA peaks in promoter extended regions were further classified in DA@TSS and DA≠TSS, depending on whether the peak was exactly (+/- 50bps) sitting at the TSS or not (based on the "distance to TSS" information reported in the annotations of the peaks). Regions considered were defined either from the center of the peaks (in the peak-centric approach) or from the TSS itself (in the genecentric approach). In that case, the coordinates of the genes were obtained with Signac method LookupGeneCoords, which returns the coordinates of the longest annotated transcript for a gene.

Motif enrichment analysis was run using the SEA tool from the MEME suite [v 5.5.5 (67, 68)] using the JASPAR CORE nonredundant database of motifs downloaded from here (69). Regions were defined the same way (that is, either from the center of the peaks in the peakcentric approach, or from the TSS in the genecentric approach), and extended by 200bp. Significance threshold was set as E-value > 10.

Coverage plots were generated using the Signac method CoveragePlot, which displays normalized signals obtained by calculating the averaged frequency of sequenced DNA fragments for the different groups of cells considered. The H3K27Ac track comes from the combination of the two replicates (18) previously mentioned.

Statistics

Data analysis and visual representation was performed with Prism 10.2 software (GraphPad) and R. Unless mentioned in the legend, all data are reported as mean \pm standard error, and dots represent individual animals. Prior to the choice of the statistical test, every dataset was tested for normality using the normal (Gaussian) distribution package included in

Prism 10.2 software (GraphPad). All details about the statistical test used, the multiple hypothesis correction, and definition of the n, are described in the figure legends. For experiments in which animals were tested across multiple behavioral sessions, repeated-measures statistical testing was applied. No statistical method was used to predetermine sample size.

REFERENCES AND NOTES

- J. L. Ronan, W. Wu, G. R. Crabtree, From neural development to cognition: Unexpected roles for chromatin. Nat. Rev. Genet. 14, 347–359 (2013). doi: 10.1038/ nrg3413; pmid: 23568486
- B. A. Olshausen, D. J. Field, Sparse coding of sensory inputs. *Curr. Opin. Neurobiol.* 14, 481–487 (2004). doi: 10.1016/ j.conb.2004.07.007; pmid: 15321069
- G. Palm, Neural associative memories and sparse coding. Neural Netw. 37, 165–171 (2013). doi: 10.1016/ j.neunet.2012.08.013; pmid: 23043727
- T. Rogerson et al., Synaptic tagging during memory allocation. Nat. Rev. Neurosci. 15, 157–169 (2014). doi: 10.1038/nrn3667; pmid: 24496410
- S. A. Josselyn, P. W. Frankland, Memory Allocation: Mechanisms and Function. Annu. Rev. Neurosci. 41, 389–413 (2018). doi: 10.1146/annurev-neuro-080317-061956; pmid: 29709212
- Y. Zhou et al., CREB regulates excitability and the allocation of memory to subsets of neurons in the amygdala. Nat. Neurosci. 12, 1438–1443 (2009). doi: 10.1038/nn.2405; pmid: 19783993
- A. P. Yiu et al., Neurons are recruited to a memory trace based on relative neuronal excitability immediately before training. Neuron 83, 722–735 (2014). doi: 10.1016/ j.neuron.2014.07.017; pmid: 25102562
- S. Duvarci, D. Pare, Amygdala microcircuits controlling learned fear. Neuron 82, 966–980 (2014). doi: 10.1016/ j.neuron.2014.04.042; pmid: 24908482
- C. Herry, J. P. Johansen, Encoding of fear learning and memory in distributed neuronal circuits. *Nat. Neurosci.* 17, 1644–1654 (2014). doi: 10.1038/nn.3869; pmid: 25413091
- C. Maison, G. Almouzni, HP1 and the dynamics of heterochromatin maintenance. Nat. Rev. Mol. Cell Biol. 5, 296–304 (2004). doi: 10.1038/nrm1355; pmid: 15071554
- X. Liu, S. Ramirez, R. L. Redondo, S. Tonegawa, Identification and Manipulation of Memory Engram Cells. Cold Spring Harb. Symp. Quant. Biol. 79, 59–65 (2014). doi: 10.1101/ sqb.2014.79.024901; pmid: 25637263
- N. L. Pettit, E.-L. Yap, M. E. Greenberg, C. D. Harvey, Fos ensembles encode and shape stable spatial maps in the hippocampus. *Nature* 609, 327–334 (2022). doi: 10.1038/ s41586-022-05113-1; pmid: 36002569
- J. E. Brownell et al., Tetrahymena histone acetyltransferase A: A homolog to yeast Gcn5p linking histone acetylation to gene activation. Cell 84, 843–851 (1996). doi: 10.1016/S0092-8674 (00)81063-6; pmid: 8601308
- M. Grunstein, Histone acetylation in chromatin structure and transcription. *Nature* 389, 349–352 (1997). doi: 10.1038/ 38664; pmid: 9311776
- J. Gräff, D. Kim, M. M. Dobbin, L.-H. Tsai, Epigenetic regulation of gene expression in physiological and pathological brain processes. *Physiol. Rev.* 91, 603–649 (2011). doi: 10.1152/ physrev.00012.2010; pmid: 21527733
- I. Ali, R. J. Conrad, E. Verdin, M. Ott, Lysine Acetylation Goes Global: From Epigenetics to Metabolism and Therapeutics. Chem. Rev. 118, 1216–1252 (2018). doi: 10.1021/acs. chemrev.7b00181; pmid: 29405707
- C. S. Park, H. Rehrauer, I. M. Mansuy, Genome-wide analysis of H4K5 acetylation associated with fear memory in mice. BMC Genomics 14, 539 (2013). doi: 10.1186/1471-2164-14-539; pmid: 23927422
- R. Halder et al., DNA methylation changes in plasticity genes accompany the formation and maintenance of memory. Nat. Neurosci. 19, 102–110 (2016). doi: 10.1038/nn.4194; pmid: 26656643
- K. K. Lee, J. L. Workman, Histone acetyltransferase complexes: One size doesn't fit all. Nat. Rev. Mol. Cell Biol. 8, 284–295 (2007). doi: 10.1038/nrm2145; pmid: 17380162
- J. Gräff, L.-H. Tsai, Histone acetylation: Molecular mnemonics on the chromatin. *Nat. Rev. Neurosci.* 14, 97–111 (2013). doi: 10.1038/nrn3427; pmid: 23324667

- C. H. Arrowsmith, C. Bountra, P. V. Fish, K. Lee, M. Schapira, Epigenetic protein families: A new frontier for drug discovery. *Nat. Rev. Drug Discov.* 11, 384–400 (2012). doi: 10.1038/ nrd3674: pmid: 22498752
- A. Hagelkruys et al., A single allele of Hdac2 but not Hdac1 is sufficient for normal mouse brain development in the absence of its paralog. *Development* 141, 604–616 (2014). doi: 10.1242/dev.100487; pmid: 24449838
- B. Yu et al., Molecular and cellular evolution of the amygdala across species analyzed by single-nucleus transcriptome profiling. Cell Discov. 9, 19 (2023). doi: 10.1038/s41421-022-00506-y; pmid: 36788214
- K. M. Tyssowski et al., Different Neuronal Activity Patterns Induce Different Gene Expression Programs. Neuron 98, 530–546.e11 (2018). doi: 10.1016/j.neuron.2018.04.001; pmid: 29681534
- H. Hochgerner et al., Neuronal types in the mouse amygdala and their transcriptional response to fear conditioning. Nat. Neurosci. 26, 2237–2249 (2023). doi: 10.1038/s41593-023-01469-3; pmid: 37884748
- J. Fernandez-Albert et al., Immediate and deferred epigenomic signatures of in vivo neuronal activation in mouse hippocampus. Nat. Neurosci. 22, 1718–1730 (2019). doi: 10.1038/s41593-019-0476-2; pmid: 31501571
- E.-L. Yap, M. E. Greenberg, Activity-Regulated Transcription: Bridging the Gap between Neural Activity and Behavior. *Neuron* 100, 330–348 (2018). doi: 10.1016/j.neuron.2018.10.013; pmid: 30359600
- A. Godino et al., Transcriptional control of nucleus accumbens neuronal excitability by retinoid X receptor alpha tunes sensitivity to drug rewards. Neuron 111, 1453–1467.e7 (2023). doi: 10.1016/j.neuron.2023.02.013; pmid: 36889314
- A. J. Rashid et al., Competition between engrams influences fear memory formation and recall. Science 353, 383–387 (2016). doi: 10.1126/science.aaf0594; pmid: 27463673
- L. Chen et al., The role of intrinsic excitability in the evolution of memory: Significance in memory allocation, consolidation, and updating. Neurobiol. Learn. Mem. 173, 107266 (2020). doi: 10.1016/j.nlm.2020.107266; pmid: 32512183
- L. A. Gouty-Colomer et al., Arc expression identifies the lateral amygdala fear memory trace. Mol. Psychiatry 21, 364–375 (2016). doi: 10.1038/mp.2015.18; pmid: 25802982
- E. Santini, G. J. Quirk, J. T. Porter, Fear conditioning and extinction differentially modify the intrinsic excitability of infralimbic neurons. *J. Neurosci.* 28, 4028–4036 (2008). doi: 10.1523/JNEUROSCI.2623-07.2008: pmid: 18400902
- Y. Y. Guo et al., Acute stress induces down-regulation of large-conductance Ca2+-activated potassium channels in the lateral amygdala. J. Physiol. 590, 875–886 (2012). doi: 10.1113/jphysiol.2011.223784; pmid: 22199169
- J.-H. Choi et al., Interregional synaptic maps among engram cells underlie memory formation. Science 360, 430–435 (2018). doi: 10.1126/science.aas9204; pmid: 29700265
- S. Nakaoka, K. Sasaki, A. Ito, Y. Nakao, M. Yoshida, A Genetically Encoded FRET Probe to Detect Intranucleosomal Histone H3K9 or H3K14 Acetylation Using BRD4, a BET Family Member. ACS Chem. Biol. 11, 729–733 (2016). doi: 10.1021/ cb501046t; pmid: 25946208
- H. Dana et al., Sensitive red protein calcium indicators for imaging neural activity. eLife 5, e12727 (2016). doi: 10.7554/ eLife.12727; pmid: 27011354
- D. J. Morrison et al., Parvalbumin interneurons constrain the size of the lateral amygdala engram. Neurobiol. Learn. Mem. 135, 91–99 (2016). doi: 10.1016/j.nlm.2016.07.007; pmid: 27422019
- T. Stefanelli, C. Bertollini, C. Lüscher, D. Muller, P. Mendez, Hippocampal Somatostatin Interneurons Control the Size of Neuronal Memory Ensembles. *Neuron* 89, 1074–1085 (2016). doi: 10.1016/j.neuron.2016.01.024; pmid: 26875623
- S. L. Klemm, Z. Shipony, W. J. Greenleaf, Chromatin accessibility and the regulatory epigenome. *Nat. Rev. Genet.* 20, 207–220 (2019). doi: 10.1038/s41576-018-0089-8; pmid: 30675018
- D. F. Clayton et al., The role of the genome in experience-dependent plasticity: Extending the analogy of the genomic action potential. Proc. Natl. Acad. Sci. U.S.A. 117, 23252–23260 (2020). doi: 10.1073/pnas.1820837116; pmid: 31127037
- P. Mews et al., Alcohol metabolism contributes to brain histone acetylation. Nature 574, 717–721 (2019). doi: 10.1038/s41586-019-1700-7; pmid: 31645761
- C. M. Greco, P. Sassone-Corsi, Circadian blueprint of metabolic pathways in the brain. *Nat. Rev. Neurosci.* 20, 71–82 (2019). doi: 10.1038/s41583-018-0096-y; pmid: 30559395

- E. Korzus et al., Transcription factor-specific requirements for coactivators and their acetyltransferase functions. Science 279, 703–707 (1998). doi: 10.1126/science.279.5351.703; pmid: 9445475
- K. Bakshi et al., Novel complex of HAT protein TIP60 and nuclear receptor PXR promotes cell migration and adhesion. Sci. Rep. 7, 3635 (2017). doi: 10.1038/s41598-017-03783-w; pmid: 28623334
- P. Thévenaz, U. E. Ruttimann, M. Unser, A pyramid approach to subpixel registration based on intensity. *IEEE Trans. Image Process.* 7, 27–41 (1998). doi: 10.1109/83.650848; pmid: 18267377
- M. Pachitariu, C. Stringer, Cellpose 2.0: How to train your own model. Nat. Methods 19, 1634–1641 (2022). doi: 10.1038/ s41592-022-01663-4; pmid: 36344832
- E. Artimovich, R. K. Jackson, M. B. C. Kilander, Y.-C. Lin, M. W. Nestor, PeakCaller: An automated graphical interface for the quantification of intracellular calcium obtained by highcontent screening. *BMC Neurosci.* 18, 72 (2017). doi: 10.1186/ s12868-017-0391-y; pmid: 29037171
- P. Rupprecht et al., A database and deep learning toolbox for noise-optimized, generalized spike inference from calcium imaging. Nat. Neurosci. 24, 1324–1337 (2021). doi: 10.1038/ s41593-021-00895-5; pmid: 34341584
- Helmchen Lab, HelmchenLabSoftware/Cascade, (2022);
 https://github.com/HelmchenLabSoftware/Cascade.
- P. Bankhead *et al.*, QuPath: Open source software for digital pathology image analysis. *Sci. Rep.* 7, 16878 (2017). doi: 10.1038/s41598-017-17204-5; pmid: 29203879
- U. Schmidt, M. Weigert, C. Broaddus, G. Myers, "Cell Detection with Star-convex Polygons" (2018; http://arxiv.org/abs/ 1806.03535) vol. 11071, pp. 265–273.
- L. Sosulina, S. Meis, G. Seifert, C. Steinhäuser, H.-C. Pape, Classification of projection neurons and interneurons in the rat lateral amygdala based upon cluster analysis. *Mol. Cell. Neurosci.* 33, 57–67 (2006). doi: 10.1016/j.mcn.2006.06.005; pmid: 16861000
- M. Tipps, E. Marron Fernandez de Velasco, A. Schaeffer, K. Wickman, Inhibition of Pyramidal Neurons in the Basal Amygdala Promotes Fear Learning. eNeuro 5, ENEURO.0272-18.2018 (2018).
- V. K. Vereczki et al., Total Number and Ratio of GABAergic Neuron Types in the Mouse Lateral and Basal Amygdala.
 J. Neurosci. 41, 4575–4595 (2021). doi: 10.1523/ JNEUROSCI.2700-20.2021; pmid: 33837051
- A. B. Chambliss, P.-H. Wu, W.-C. Chen, S. X. Sun, D. Wirtz, Simultaneously defining cell phenotypes, cell cycle, and chromatin modifications at single-cell resolution. FASEB J. 27, 2667–2676 (2013). doi: 10.1096/fj.12-227108; pmid: 23538711
- M. Y. Batiuk et al., Upper cortical layer-driven network impairment in schizophrenia. Sci. Adv. 8, eabn8367 (2022). doi: 10.1126/sciadv.abn8367; pmid: 36223459
- Y. Hao et al., Integrated analysis of multimodal single-cell data. *Cell* 184, 3573–3587.e29 (2021). doi: 10.1016/ j.cell.2021.04.048; pmid: 34062119
- T. Stuart, A. Srivastava, S. Madad, C. A. Lareau, R. Satija, Single-cell chromatin state analysis with Signac. *Nat. Methods* 18, 1333–1341 (2021). doi: 10.1038/s41592-021-01282-5; pmid: 34725479
- T. P. O'Leary et al., Extensive and spatially variable within-cell-type heterogeneity across the basolateral amygdala. eLife 9, e59003 (2020). doi: 10.7554/eLife.59003; pmid: 32869744
- M. Andreatta, S. J. Carmona, UCell: Robust and scalable singlecell gene signature scoring. *Comput. Struct. Biotechnol. J.* 19, 3796–3798 (2021). doi: 10.1016/j.csbj.2021.06.043; pmid: 34285779
- A. M. Burns et al., The HDAC inhibitor CI-994 acts as a molecular memory aid by facilitating synaptic and intracellular communication after learning. Proc. Natl. Acad. Sci. U.S.A. 119, e2116797119 (2022). doi: 10.1073/pnas.2116797119; pmid: 35613054
- 62. Merging objects. https://stuartlab.org/signac/articles/merging.
- Y. Zhang et al., Model-based analysis of ChIP-Seq (MACS).
 Genome Biol. 9, R137 (2008). doi: 10.1186/gb-2008-9-9-r137;
 pmid: 18798982
- G. Yu, L.-G. Wang, Q.-Y. He, ChlPseeker: An R/Bioconductor package for ChlP peak annotation, comparison and visualization. *Bioinformatics* 31, 2382–2383 (2015). doi: 10.1093/ bioinformatics/btv145; pmid: 25765347
- T. Wu et al., clusterProfiler 4.0: A universal enrichment tool for interpreting omics data. *Innovation (Camb.)* 2, 100141 (2021). doi: 10.1016/j.xinn.2021.100141; pmid: 34557778

- Stuart Lab, signac/R/utilities.R, GitHub (2023); https://github. com/stuart-lab/signac/blob/ e65a74dbe8e489f92b01a2a9c049c67a317c83a0/R/utilities.R.
- T. L. Bailey, C. E. Grant, SEA: Simple Enrichment Analysis of motifs. bioRxiv 2021.08.23.457422 [Preprint] (2021). doi: 10.1101/2021.08.23.457422
- T. L. Bailey, J. Johnson, C. E. Grant, W. S. Noble, The MEME Suite. Nucleic Acids Res. 43, W39-49 (2015). doi: 10.1093/nar/ gkv416; pmid: 25953851
- T. L. Bailey, W. S. Noble, MEME Suite Releases (2023); https://meme-suite.org/meme/meme-software.
- M. Leleu, BICC-UNIL-EPFL/MultiOmics_HATs: v1.0, Zenodo (2024); https://zenodo.org/records/11125098.
- S. Zamora, SimonZamora/Santoni_2024_CalciumImaging FRETAnalysis: Materials_Methods_Santoni2024: v1.0, Zenodo (2024); https://zenodo.org/records/11125607.

ACKNOWLEDGMENTS

We thank all past and current members of the Laboratory of Neuroepigenetics for fruitful discussions and comments pertaining to the advancement of this project, in particular B. A. Silva and J. V. Sanchez-Mut for their invaluable knowledge and technical insights, and A. B. Marques and H. M. Vernon for their contributions in

histological procedures and confocal imaging analysis. We also thank EPFL's Center of Phenogenomics for ensuring the welfare of the laboratory animals, the Bioimaging and Optic Core Facility for their technical assistance with experiment planning and image analysis, C. Iseli and N. Guex from the Bioinformatics Competence Center for their technical advice with the multiomics analysis, the Gene Expression Core Facility for their technical assistance with experiment planning and sequencing, and the Histology core Facility for their technical support. All data are available in the manuscript, the supplementary material or deposited at GEO DataSets database and Zenodo (70, 71). Funding: This work was supported by the European Research Council grant ERC StG 678832, the Swiss National Science Foundation SNSF 197752, and NCCR Synapsy PH02P35 (to J.G.); and by the Swiss National Science Foundation SNSF 176206, 197942, and NCCR Synapsy 51NF40-185897 (to C.S.). Author contributions: G.S. performed all mouse surgeries and behaviors, cellular, and molecular procedures, and data analysis; S.A. performed the patch-clamp experiments; M.L. performed the analysis of the multiomics datasets; L.G. performed cloning and viral production; S.A.Z. performed the FRET-Calcium imaging and data processing; M.S. performed histological procedures and shHAT-related analysis, and I.T. performed morphological spine imaging and analysis. C.S. supervised the patch-clamp experiments

and experimental design; J.G. supervised the entire project. The manuscript was written by G.S. and J.G. and commented on by all authors. Competing interests: Authors declare that they have no competing interests. Data and materials availability: All data are available in the main text or the supplementary materials. For sn-MultiOmics data refer to GEO accession GSE220696 (see supplementary materials) and to (70) for data analysis pipeline. For combined FRET-calcium recordings analysis pipeline refer to (71). License information: Copyright © 2024 the authors, some rights reserved; exclusive licensee American Association for the Advancement of Science. No claim to original US government works. https://www.science.org/about/science-licenses-journal-article-reuse

SUPPLEMENTARY MATERIALS

science.org/doi/10.1126/science.adg9982 Figs. S1 to S12 Tables S1 to S8

MDAR Reproducibility Checklist Data S1 to S5

Submitted 3 February 2023; resubmitted 1 March 2024 Accepted 24 May 2024 10.1126/science.adg9982